

UNIVERSITY of CALIFORNIA
SANTA CRUZ

**THE EFFECTS OF BACKGROUND MAGNETIC FIELDS ON
ASTROPHYSICAL FINGERING CONVECTION**

A thesis submitted in partial satisfaction of the
requirements for the degree of

MASTER OF SCIENCE

in

SCIENTIFIC COMPUTING & APPLIED MATHEMATICS

by

Peter Z. Harrington

December 2018

The thesis of Peter Z. Harrington is approved:

Professor Pascale Garaud, Chair

Professor Nicholas Brummell

Professor Dongwook Lee

Lori Kletzer
Vice Provost, Dean of Graduate Studies

Copyright © by
Peter Z. Harrington
2018

Contents

List of Figures	iv
List of Tables	vi
Acknowledgements	viii
1 Introduction & Background	1
1.1 The double-diffusive instability & fingering convection	1
1.2 Astrophysical scenarios: low Prandtl number	4
1.2.1 Fingering convection in stars	5
1.2.2 The need for new physics	7
1.3 Development of mathematical model	10
2 Numerical tool: PADDIM	16
2.1 PADDIM design overview	17
2.1.1 Physical model	17
2.1.2 Numerical scheme	18
2.2 Verification & Testing	20
2.2.1 Magnetic diffusion	21
2.2.2 Velocity-induced magnetic field	21
2.2.3 Lorentz force	23
3 Linear stability analysis	26
3.1 Region of instability and fastest-growing modes	28
3.2 Verification via DNS	30
4 Numerical Simulations	35
4.1 Qualitative Results	36
4.1.1 Horizontal background fields	36
4.1.2 Vertical background fields	39
4.2 Analytical model for the vertical field case	41
5 Discussion	47
A	49

List of Figures

2.1	The numerical results for the vertical profile of the x -component of the magnetic field at several time steps during the magnetic diffusion test. The profile of each time step plotted is colored according to simulation time, with blue corresponding to $t = 0$ and red corresponding to the end of the simulation.	22
2.2	The numerical results for the vertical profile of the x -component of the magnetic field at several time steps during the Laminar flow kinematic dynamo test. The profile of each time step plotted is colored according to simulation time, with blue corresponding to $t = 0$ and red corresponding to the end of the simulation.	23
2.3	The numerical results (red) and the analytical linearized solutions (blue) for the vertical profiles of the y -component of the magnetic field (left) and the velocity field (right) at several time steps during the Alfvén wave test.	25
3.1	Maximum real part of all roots of the growth rate polynomial in Eq. (3.14) as a function of horizontal wave number \hat{k}_H and vertical wave number \hat{k}_z , for a background magnetic field along the z -direction with intensities corresponding to (a) $H_B = 0.01$ and (b) $H_B = 1$. The other parameters are $\text{Pr} = \tau = \text{D}_B = 0.1$, $R_0 = 1.45$ for both plots, and red colors indicate instability.	29
3.2	Surfaces of null stability for background magnetic field inclinations of $\theta \in \{0, \pi/6, \pi/3, \pi/2\}$ at $H_B = 1$. The background field is chosen, without loss of generality, to have no component along the y direction. Artificial lighting is included to render the bumps in the surface.	31
3.3	The kinetic (“K”, solid lines) and magnetic (“M”, dashed lines) energies as a function of time (in units of the thermal diffusion timescale) for simulations with the background magnetic field aligned along the z -direction. The background field strengths in each run correspond to $H_B = 0.01$ (red), $H_B = 0.1$ (green), $H_B = 1$ (blue), $H_B = 10$ (purple), and $H_B = 100$ (orange).	32
3.4	Two snapshots of the compositional perturbations in the x - z plane taken at early times in simulations with a vertical background magnetic field. The left panel shows a weak-field case, with $H_B = 0.01$, while the right panel shows how a stronger field, with $H_B = 1$, makes the finger structure more dominated by the $\hat{k}_z = 0$ “elevator modes”. Color scale runs from -0.036 (blue) to +0.036 (red) on the left, and from -1.20 (blue) to 1.20 (red) on the right, both in non-dimensional units.	33
3.5	Two snapshots of the compositional field in the x - y plane taken at early times in a simulation with a horizontal background magnetic field (a) and a vertical background magnetic field (b). Color scale runs from -20 (blue) to +20 (red) in non-dimensional units.	34

4.1	The evolution of the kinetic (solid lines, “K”) and magnetic (dashed lines, “M”) energies over time (in units of the thermal diffusion timescale) for horizontal magnetic field simulations with $H_B = 0.01$ (orange), $H_B = 0.1$ (cyan), and $H_B = 10$ (blue). Also plotted is a simulation with $H_B = 10$ and a field inclined 45° from the z -axis (purple, “inc”). The trajectory of the kinetic energy for the $H_B = 0.01$ case is qualitatively identical to that of the non-magnetic case.	37
4.2	Sample visualizations of the vertical fluid velocity component for runs with $H_B = 10$. At left, we show a case with the background field inclined at an angle of $\theta = \pi/4$ from the z -axis, and at right we show a case with a fully-horizontal field (which required extending the vertical extent of the simulation domain considerably), long after the instability has surpassed the saturation “peak” of the initial instability.	38
4.3	Visualizations of the vertical fluid velocity component during the post-saturation, statistically stationary state, for runs with a vertical background field and $H_B = 0.01$ (left), $H_B = 1$ (middle), and $H_B = 10$ (right). Increasing the strength of the magnetic field (via H_B) imparts greater vertical coherence to the fingering structures.	40
4.4	The compositional Nusselt number Nu_C (see Eq. (4.1)) as a function of time (in units of the thermal diffusion timescale) in simulations with a vertical field for various values of H_B . The dashed purple line shows the case with an inclined background field, and the black dashed-line shows a non-magnetic simulation ($H_B = 0$).	41
4.5	The non-dimensional growth rate of the shear instability $\hat{\sigma}$ as a function of H_B^* (blue crosses). The red line shows the fit given by Eq. (4.5).	43
4.6	The volume-averaged squared vertical velocity $\langle u_z^2 \rangle$ (left, green squares) and compositional Nusselt number Nu_C (right, green triangles) as a function of H_B from the simulations. The different lines show the prediction from Eq. (4.7) for $\hat{\lambda}_f = 0.147$ (black), corresponding to the parameters in the simulations; $\hat{\lambda}_f = 10^{-3}$ (blue), representative of a white dwarf’s fingering convection environment; and $\hat{\lambda}_f = 10^{-5}$ (red), representative of an RGB star’s fingering convection environment.	44
A.1	Schematic of the two-dimensional sinusoidal shear flow considered in the Floquet analysis of magnetized shear between fingers.	49

List of Tables

1.1	Order-of-magnitude estimates for various governing parameters within the expected fingering convection regions of Main Sequence stars, Red Giant Branch stars, and White Dwarfs. The ranges represent values from the lower radius to the upper radius of the fingering region. All units are in cgs.	15
2.1	The meaning of the parameters in Eqs. (2.1) - (2.5). The coefficients of various terms (e.g. D_u , H_B , etc) are written as such to support many different possible non-dimensionalizations.	18

Abstract

The Effects of Background Magnetic Fields on Astrophysical Fingering Convection

by

Peter Z. Harrington

Double-diffusive convection at higher Prandtl numbers ($\text{Pr} \sim O(1)$ or larger) has been well studied in geophysical contexts, but detailed investigations of the low Prandtl number regimes ($\text{Pr} \ll 1$) which are relevant to most astrophysical scenarios like stellar or planetary interiors have only recently become feasible. Since most low-Pr fluids in astrophysical scenarios are electrically conducting, it is possible that magnetic fields play a role in either enhancing or suppressing double-diffusive convection, but to date there have been no numerical investigations of such possibilities. Here we study the effects of both vertical (aligned with the gravitational axis) and horizontal background magnetic fields on the linear stability and nonlinear saturation of double-diffusive convection, through a combination of theoretical work and direct numerical simulation (DNS). Both vertical and horizontal background magnetic fields are found to significantly enhance the saturation and post-saturation values of fluid kinetic energy, vertical motion, and chemical flux relative to standard fingering convection, but the two cases differ considerably in their behavior. We focus mainly on the vertical case, finding that a vertical magnetic field suppresses the secondary shear instabilities between up- and down-flowing fingers such that saturation of the instability is delayed until significantly higher levels of vertical fluid motion are reached. This allows magnetized fingering convection to have significantly enhanced levels of turbulent mixing of chemical species with respect to the hydrodynamic case. Consequentially, magnetic effects offer a promising explanation of discrepancies between theoretical and observed mixing rates in low-mass red giant branch (RGB) stars.

Acknowledgements

I need to acknowledge the exceptional efforts of my thesis advisor, Dr. Pascale Garaud, who spent countless hours with me working on this project and showed a remarkable dedication to my personal and professional development. I have learned so much, thanks to her willingness to explain every last detail I was curious about, and am extremely grateful for the opportunities and connections she has provided for me. Her invitation for me to spend a month in Woods Hole at the Geophysical Fluid Dynamics program ended up providing me with an experience that was somehow relaxing and highly productive at the same time, and her encouragement (and guidance) in my participation at the DFD meeting as well as in writing up our results for publication allowed me to surpass the limits of my own expectations. It also goes without saying that the completion of this project would not have been possible without the generous financial support she was able to secure for me.

I want to extend additional thanks to Dr. Nicholas Brummell, Dr. Dongwook Lee, and Dr. Shawfeng Dong for their excellent instruction in the fundamentals that preceded my work on this project – magnetohydrodynamics, numerical computing in Fortran, and high-performance computing. I benefited greatly from their technical expertise and their ability to simplify complex topics. Dr. Brummell’s course gave me a strong intuitive understanding of the MHD equations, which was extremely helpful when trying to understand the physical behavior I observed in my simulations. The simulations themselves would not have been possible had I not been given an excellent preparation, first in Dr. Lee’s numerical linear algebra course and then in Dr. Dong’s HPC course, in modern Fortran and standard HPC techniques.

I would also like to acknowledge the dedication (and patience) shown by Dr. Dong and Dr. Robert Brant in their involvement with the UCSC Hyades compute cluster, on which I ran all of my simulations. Hyades was purchased with an NSF MRI grant (AST-1229745), and this work was funded in part by NSF-AST 1412951 and 1517927. Lastly, thanks to Sutirtha Sengupta, soon-to-be PhD, for his advice, guidance, camaraderie and eagerness to commiserate about troubles with VisIt.

1 Introduction & Background

1.1 The double-diffusive instability & fingering convection

The double diffusive instability has long served the field of fluid dynamics as a rich and interesting phenomenon, with significant implications for physical processes observed both on Earth as well as in more distant corners of the universe. Because the field has grown substantially since its inception, there are now many systems in which double-diffusive instabilities have been found to play a major role in the overall dynamics. Applications have been found in oceanography, astrophysics, geophysics, and industrial engineering. The wide variety of contexts in which double-diffusive instabilities are relevant corresponds to some diversity in both the physical parameters and the resulting behaviors of these systems, but they all depend on the same underlying idea – if the density of a fluid depends on two components which diffuse at different rates, then the fluid may be unstable under the influence of gravity even when its net density stratification is stable. The two components truly can be anything affecting the density of the fluid (i.e., any quantity that changes the buoyancy when its concentration increases or decreases), but the most typical ones are temperature and chemical composition.

The double-diffusive instability was first discovered and modeled in the context of the ocean, where heat and salt both affect the density of ocean water but heat diffuses at a rate which is two orders of magnitude faster than salt. Stommel et al. (1956) were the first to propose that sustained fluid motion could be generated by arranging warm, salty water over cold, fresh water, as

long as a vertical salinity gradient could be maintained in the system. However, they did not fully recognize that the key ingredient was the difference in diffusivities between heat and salt. This was done in a seminal work by Stern (1960), which laid out the mathematical details for the first model of the double-diffusive instability, and correctly predicted that conditions in the ocean could sustain it.

Stern (1960) focused on the branch of double-diffusion known as fingering convection (also called thermohaline convection, as Stern named it in the title of the original paper), named for the long, thin vertical structures formed by the instability. The mechanism for fingering convection is most easily imagined within the heat and salt framework in which it was originally described – picture an arrangement of hot, salty water on top of cold, fresh water, such that both components have (roughly constant) vertical gradients. Without the thermal gradient to compensate and make the fluid less dense on top, the upper regions of salty water would be overdense, and would begin sinking via the Rayleigh-Taylor instability. However, the increased heat (thus decreased density) on top counteracts the increased salinity and makes the fluid bottom-heavy, which we would naively assume to be dynamically stable. This stable density stratification is a rather non-intuitive aspect of the fingering instability, since we wouldn't ordinarily expect a bottom-heavy fluid initially at rest to begin spontaneously moving. However, if a small parcel of fluid is perturbed downwards, its temperature will equilibrate with the colder surrounding fluid much faster than its salinity will, due to the higher diffusivity of heat. Then, the displaced parcel of fluid is now overdense – it still has a higher salinity than its surroundings – and continues to sink downwards.

The mechanism works in the reverse direction, where fluid perturbed upwards will equilibrate in temperature and become underdense due to its lack of salinity, thus driving further upward buoyant motion. The upward and downward motion of parcels of fluid form the long, vertical fingers for which the fingering instability is named, and the energy source driving this motion is the potential energy stored in the top-heavy salinity distribution. This example described the two diffusers as heat and salt, but is easily generalized to any two quantities that both affect the local density of the

fluid. The configuration which defines fingering convection is simply one where the faster diffuser is stabilizing (e.g., hot water on top of cold water) and the slower diffuser is de-stabilizing (e.g., salty water on top of fresh water).

The other branch of the double-diffusive instability, one that is essentially a “mirror image” of fingering convection, is known as oscillatory double-diffusive convection (ODDC, also referred to as diffusive convection, and in stellar physics, semiconvection; e.g., Baines and Gill, 1969; Kato, 1966; Spiegel, 1969). This occurs when the faster diffuser is destabilizing and the slower diffuser is stabilizing (e.g., cold, fresh water over hot, salty water), where the motion induced by the instability causes perturbed parcels of fluid to undergo an overstable oscillation. While perhaps being slightly less well-studied than fingering convection, ODDC still has important implications for both geophysical and astrophysical scenarios.

Both fingering convection and ODDC significantly enhance mixing within their environments, by increasing the vertical turbulent transport of heat or chemical species. Also, depending on the values of various governing parameters, they can both lead to the formation of significant secondary instabilities or large-scale structures within their environments after the initial instability saturates. The fingering instability can lead to the development of large-scale gravity waves through a mechanism called the collective instability (Stern, 1969; Stern and Turner, 1969), which further enhances turbulent chemical transport. Fingering convection can also eventually form distinct layers of fluid, stacked on top of each other and separated by thin interfaces, by the so-called γ -instability (Radko, 2003). This mechanism for layer formation was confirmed by numerical simulations of fingering convection (e.g., Stellmach et al., 2011), and it was shown by Traxler et al. (2011) that the collective instability and the γ -instability are just different unstable modes of the same mean-field equations. The formation of layers in ODDC has also been observed in both laboratory experiments (e.g., Turner, 1965) as well as the ocean (e.g., Timmermans et al., 2003). In the ocean, for both ODDC as well as fingering convection, the formation of layers creates “thermohaline staircases” (e.g., Schmitt et al., 1987), which further enhance the turbulent vertical transport of chemical species

(Schmitt et al., 2005).

1.2 Astrophysical scenarios: low Prandtl number

The geophysical contexts in which double-diffusion was first studied all share a common region of parameter space, where the Prandtl number $\text{Pr} = \nu/\kappa_T$ is of order one or larger. This means that viscosity plays an important role in dictating the dynamics for such systems. However, in astrophysical contexts, this is not the case. Liquid metals like those found in planetary interiors have $\text{Pr} \sim 10^{-3} - 10^{-1}$, and the plasmas found in stellar interiors can have $\text{Pr} \sim 10^{-9} - 10^{-5}$, because electron conduction in liquid metals and photon transport in plasmas allow the fluid to thermally equilibrate much more rapidly. As a result, viscous diffusion becomes negligible on the length scales associated with double-diffusive convection, making the dynamics more strongly dominated by inertial terms.

Unfortunately, laboratory experiments reproducing the low-Pr conditions of astrophysical double-diffusive convection are all but impossible. Furthermore, the extremely low values that of Pr in astrophysical environments make numerical simulations very computationally expensive. Indeed, 3D direct numerical simulations (DNSs) of low-Pr double-diffusive fluids have only become feasible within the last decade or so, and even with current technology, modeling the behavior for systems with $\text{Pr} < \sim 10^{-3}$ remains a challenge. Nonetheless, DNSs have become the most important tool in studying these systems, as they allow us to observe in great detail the growth of the instability, its nonlinear saturation, and post-saturation behavior, which would otherwise be scientifically inaccessible.

As a result of the difficulties associated with the low-Pr regime, working out the details of double diffusive convection with $\text{Pr} \leq 0.3$ is an on-going problem (see Garaud, 2018, for an in-depth review). There are quite a few similarities between the high- and low-Pr regimes of double-diffusive convection, and some key differences as well. A major finding is that the γ -instability, which can lead to layer formation in both fingering convection and ODDC, is suppressed for fingering convection in

the low- Pr regime, since the turbulent fluxes of heat and composition remain small (Garaud et al., 2015). The same study found that the collective instability, which can also lead to layering, is also suppressed for $\text{Pr} \leq 10^{-3}$, which precludes stellar environments. On the other hand, ODDC at low Prandtl number has been shown to have a relatively large range of parameter space where layer formation is likely (Mirouh et al., 2012), with the γ -instability of Stern (1969) being the mechanism by which layers form (Rosenblum et al., 2011). We will now focus solely on fingering convection, and in particular, the type expected to occur in stellar environments.

1.2.1 Fingering convection in stars

Relatively soon after the first studies of fingering convection were published, Spiegel (1969) was the first to review the applicability of double-diffusive instabilities to stellar environments. Because the field of fingering convection was still in its early days, having just developed from the “salt-finger” framework of Stern (1960), stellar fingering convection was also dubbed “thermohaline convection” (as Stern (1960) called it in his original paper), despite the absence of salt in stellar environments. This practice has continued even into the present day, but we will refer to the phenomenon solely as fingering convection. As Spiegel (1969) noted, most stellar interiors, or at least parts of them, possess the basic ingredients required for double-diffusive convection – stratified fluid, with vertical gradients in both heat and chemical composition, and a thermal diffusivity much larger than the compositional diffusivity. The key “catalyst” required to initiate fingering convection is that the compositional stratification must be unstable within the region under consideration. Because heavier elements are mainly found near the center of stars (as the majority of stellar nuclear reactions are fusion reactions occurring in the core), the mean molecular weight of the fluid is, in general, stably stratified. Thus, the unstable compositional gradients needed for fingering convection only arise in certain situations where localized inversions of this compositional gradient occur.

There are multiple scenarios where this unstable compositional gradient (sometimes referred to as a “ μ -inversion”) may arise, all of which occur away from the center of the star. The most

obvious way of increasing the mean molecular weight at larger stellar radii is via the accretion of heavy material onto the surface. This material can come from planetary material (Vauclair, 2004; Garaud, 2011; Théado and Vauclair, 2012), an evolved companion in a binary system (Stothers and Simon, 1969; Stancliffe et al., 2007), or a disk of debris nearby a white dwarf (WD) star (Deal et al., 2013). In these scenarios, fingering convection would then occur at the surface of the star, lasting until the heavy elements are drained away from the surface such that the unstable compositional gradient disappears. A rather less obvious way of developing an unstable compositional gradient is via the transport of heavy elements, the most commonly cited being iron, through a combination of atomic diffusion and radiative levitation (Théado et al., 2009; Zemsanova et al., 2014). These processes can transport heavier elements from the deeper interior of the star upwards, forming layers of heavy fluid at larger radii, which can then lead to fingering convection. As in the case of surface accretion, the mixing induced by fingering convection would then begin to dissipate the accumulated heavier layer of fluid (however, helium settling has been shown to partially suppress this dissipation, see Zemsanova et al., 2014).

Besides accretion and atomic diffusion, a third way of developing the required unstable compositional gradient is via off-center burning – these cases are characterized by rare nuclear reactions, occurring away from the stellar core, which modify the local mean molecular weight of the fluid. By far the most well-studied example of such a scenario is the ${}^3\text{He}+{}^3\text{He} \rightarrow {}^4\text{He}+\text{p}+\text{p}$ reaction (initially pointed out to be relevant to stellar fingering convection by Ulrich, 1972), which occurs near the edge of the hydrogen-burning shell in red giant branch (RGB) stars. As this reaction locally reduces the mean molecular weight of the fluid, fingering convection begins to occur just above the shell, eventually spanning the entirety of the region between the shell and the convective zone of the star.

1.2.2 The need for new physics

The study of stellar fingering convection has always involved a focus on how much it could contribute to the mixing of chemical species within a star (the transport of heat is not as significant since the molecular thermal diffusivity κ_T is so large in stellar interiors). Quantifying this mixing was a central focus of the efforts of Ulrich (1972), who developed a prescription for chemical mixing in the context of fingering convection within RGB stars. Later, Kippenhahn et al. (1980) developed a very similar model, which effectively only differed from the model of Ulrich (1972) by a multiplicative constant C_M .

In RGB stars, canonical models of mixing (which ignore fingering convection) do not predict any variations in the surface abundances of heavy elements after the so-called “first dredge-up”, which happens when the star evolves from the main sequence (MS) onto the RGB. However, Gratton et al. (2000) observed such variations in stars evolving up the RGB, finding post-dredge-up evolution in the abundances of lithium and chemical by-products of the CNO cycle. This pointed to the presence of some unknown mixing process, and Charbonnel and Zahn (2007a) were the first to attribute these observations to fingering convection of the type likely to occur in RGB stars. They point out that since the RGB fingering convection region is near the edge of the hydrogen burning shell, the onset of the instability brings the possibility of mixing heavier elements (fusion reaction products and by-products) from deep within the star up into the convective zone, which would eventually circulate them to the surface where they would be spectroscopically detectable. By a similar process but in the opposite direction, lithium from the surface can be mixed down through the convective zone and then transported by fingering convection down to deep enough levels where it is destroyed, thus decreasing its spectroscopic signature at the surface.

Towards explaining the observations of Gratton et al. (2000), Charbonnel and Zahn (2007a) adapted a stellar evolution code to implement the mixing prescriptions of both Ulrich (1972) and Kippenhahn et al. (1980), finding the observations well-accounted for provided $C_M \sim 1000$ as prescribed by Ulrich (1972). However, 3D DNSs of fingering convection (Denissenkov, 2010; Traxler

et al., 2011; Brown et al., 2013) all agree that $C_M \sim 10$ or less, representing a difference between theoretical and observed mixing rates in fingering convection of two orders of magnitude (see, for example, Wachlin et al., 2014).

This “missing-mixing” problem in RGB stars is at the heart of current research in astrophysical fingering convection, as there is a clear need to introduce novel effects into the basic model in order to explain observations. As mentioned previously, the formation of layers in both laboratory and oceanic fingering convection is well-known to greatly enhance chemical transport, so Brown et al. (2013) and Garaud et al. (2015) investigated the possibility of such layer formation in stellar fingering convection but found that it could not occur in the regime of parameters relevant to RGB stars. Recently, Sengupta and Garaud (2018) studied the effect of rotation on fingering convection as a possible solution to the issue. Contrary to their expectations, they found that rotation actually slightly reduced the amount of mixing, except for one case where a large-scale vortex (LSV) developed, which greatly enhanced mixing. The emergence of the LSV in the work of Sengupta and Garaud (2018) may thus explain, or partially explain, the missing mixing problem, but it also bears a number of caveats – among them, that vortex formation in rotating DNSs appears to depend on both the horizontal aspect ratio of the domain (Julien et al., 2018) and the latitude of the region considered (Moll and Garaud, 2017).

What has been left relatively untouched so far, especially in terms of DNSs, is the effect of magnetic fields. While many stellar models rely on hydrodynamic approximations, the electrical conductivity of plasmas in stars makes the true physical behavior intrinsically magnetohydrodynamic (MHD), but there have been few attempts to model MHD fingering convection in detail. A study of stellar double-diffusive MHD instabilities was done by Hughes and Weiss (1995), who investigated the case where magnetic buoyancy, resulting from a stratified background magnetic field, would act analogously to the compositional buoyancy (slow diffuser) in standard thermocompositional fingering. They proposed this as a mechanism to explain evolution of the solar magnetic field, and the formation of active regions and sunspots, finding that even in the case where the background gradients in both

the temperature and magnetic fields are stabilizing, steady convection can still occur. More recently, Charbonnel and Zahn (2007b) proposed that the small percentage of RGB stars which do not show extra mixing (in contrast to the vast majority that do) might be explained by the presence of a strong toroidal magnetic field (by their estimate, around 10^5 G) that could inhibit the onset of fingering convection. Their proposal was based on a local linear analysis and neglected the nonlinear behavior of the instability. More on this will be discussed in Section 3. In contrast, Denissenkov et al. (2009) proposed that a strong toroidal magnetic field component (around $10^5 - 10^7$ G) would enhance chemical mixing via a mechanism they called “magneto-thermohaline mixing”, wherein buoyant magnetic flux rings formed by differential rotation in the region where fingering convection was taking place would rise up and increase the vertical transport of chemical species. However, this one-dimensional model bears a number of constraints on the local conditions within RGB stars which are difficult to verify, especially for the vast majority of RGB stars that show enhanced mixing rates (they call for 3D numerical simulations to resolve these issues).

It is thus clear that an in-depth theoretical analysis (and particularly, a dedicated 3D DNS campaign) of MHD fingering convection would be both a novel step and one that has the potential to resolve significant issues with stellar fingering convection. This work is a first crack at the problem, and has three principal goals:

1. To develop a reasonable model for MHD fingering convection in the presence of constant background magnetic fields, and study the linear stability of the model to investigate what effects a magnetic field could have on the basic instability.
2. To run a suite of 3D numerical simulations, investigating the nonlinear saturation and post-saturation behavior of the instability, for a variety of field strengths and configurations.
3. To investigate the impact of magnetic fields on vertical fluxes of heat and composition by fingering convection.

We now focus on the first of these goals, and derive our base mathematical model. Then, in Section

2, we will describe the numerical tool developed to perform DNSs of MHD fingering convection. In Section 3, we will present and discuss the linear stability of our model, and in Section 4, we will present the numerical simulations and develop an analytical model for some of our results. Finally, we will discuss implications and conclude in Section 5.

1.3 Development of mathematical model

We consider a Cartesian domain and assume that the fluid satisfies the Boussinesq approximation (Spiegel and Veronis, 1960). This is a standard step taken in setting up the fingering convection system, and is a good approximation for stellar interiors (as well as oceanic environments) because typical root mean square velocities are much less than the sound speed and the size of the region being modeled is much less than the pressure and density scale heights. An implicit assumption in following the Boussinesq approximation and not its magneto-Boussinesq variant is that we are neglecting magnetic buoyancy effects, as we will study the scenario where the background magnetic field is constant within the domain.

The base set of equations are

$$\nabla \cdot \mathbf{u} = 0 \quad (1.1)$$

$$\rho_m \left(\frac{\partial \mathbf{u}}{\partial t} + \mathbf{u} \cdot \nabla \mathbf{u} \right) = -\nabla p + \rho_m \nu \nabla^2 \mathbf{u} + \frac{1}{\mu_0} (\nabla \times \mathbf{B}) \times \mathbf{B} + \rho' \mathbf{g} \quad (1.2)$$

$$\frac{\partial T}{\partial t} + \mathbf{u} \cdot \nabla T - u_z \frac{dT_{\text{ad}}}{dz} = \kappa_T \nabla^2 T \quad (1.3)$$

$$\frac{\partial C}{\partial t} + \mathbf{u} \cdot \nabla C = \kappa_C \nabla^2 C \quad (1.4)$$

$$\frac{\partial \mathbf{B}}{\partial t} = \nabla \times (\mathbf{u} \times \mathbf{B}) + \eta \nabla^2 \mathbf{B} \quad (1.5)$$

$$\nabla \cdot \mathbf{B} = 0 \quad (1.6)$$

where $\mathbf{u} = (u_x, u_y, u_z)$ is the fluid velocity, $\mathbf{B} = (B_x, B_y, B_z)$ is the magnetic field, ρ_m is the reference density, ρ' are perturbations away from ρ_m , p is the pressure, g is the local gravity, T

is the temperature field, and C is the compositional field, which can either represent the mean molecular weight of the fluid, or the concentration of a particular chemical species. The vertical adiabatic temperature gradient $\frac{dT_{\text{ad}}}{dz}$ is equal to $-\frac{g}{c_p}$, where c_p is the specific heat at constant pressure of the fluid. This must be included to account for the intrinsic thermodynamic structure in the star. The kinematic viscosity ν , and the thermal, compositional, and magnetic diffusivities, κ_T , κ_C , and η , respectively, are assumed to be constant. Here we assume that the magnetic permeability μ_0 is simply that of a vacuum, which is equal to 4π in cgs units. Equation (1.1) is the continuity equation, Eq. (1.1) is the Navier-Stokes equation with body forces of gravity and the Lorentz force, Eqs. (1.3)-(1.4) are advection-diffusion equations for thermal and compositional fields, respectively, Eq. (1.5) is the induction equation, and Eq. (1.6) is the divergence-free constraint associated with the magnetic field.

Following the Boussinesq approximation dictates that variations in the fluid density only affect the dynamics via thermal or compositional buoyancy (i.e., only from the \mathbf{g} term and not in the others in Eq. 1.2). We then use a linearized equation of state such that the density perturbations ρ' with respect to the reference value ρ_m satisfy

$$\frac{\rho'}{\rho_m} = -\alpha T' + \beta C', \quad (1.7)$$

where T' and C' are perturbations to their respective background fields, such that $T = T_m + T'$ and $C = C_m + C'$, where T_m and C_m are constant. The coefficients α and β are constants of thermal expansion and compositional contraction, respectively, given by

$$\alpha = -\frac{1}{\rho_m} \frac{\partial \rho}{\partial T} \Big|_{p,C}, \quad \beta = \frac{1}{\rho_m} \frac{\partial \rho}{\partial C} \Big|_{p,T}. \quad (1.8)$$

Since the region under consideration is small compared to thermocompositional scale heights, we then assume the existence of a constant background gradient along the vertical direction for both the thermal and compositional field (e.g., Baines and Gill, 1969), such that

$$T' = z \frac{dT_0}{dz} + \tilde{T}, \quad (1.9)$$

$$C' = z \frac{dC_0}{dz} + \tilde{C}. \quad (1.10)$$

We assume that the perturbations \tilde{T} and \tilde{C} , as well as \mathbf{u} and \mathbf{B} , are triply-periodic in the domain.

With these assumptions in place, the thermal and compositional equations reduce to

$$\frac{\partial T'}{\partial t} + \mathbf{u} \cdot \nabla T' + u_z \left(\frac{dT_0}{dz} - \frac{dT_{\text{ad}}}{dz} \right) = \kappa_T \nabla^2 T', \quad (1.11)$$

$$\frac{\partial C'}{\partial t} + \mathbf{u} \cdot \nabla C' + u_z \frac{dC_0}{dz} = \kappa_C \nabla^2 C', \quad (1.12)$$

while the velocity equation becomes

$$\frac{\partial \mathbf{u}}{\partial t} + \mathbf{u} \cdot \nabla \mathbf{u} = -\frac{1}{\rho_m} \nabla p + \nu \nabla^2 \mathbf{u} + \frac{1}{\mu_0 \rho_m} (\nabla \times \mathbf{B}) \times \mathbf{B} + (\alpha T' - \beta C') g \hat{\mathbf{e}}_z. \quad (1.13)$$

The magnetic induction equation is not directly affected by the previous assumptions, and thus it is unchanged.

The standard non-dimensionalization chosen for fingering convection is based on the length scale d associated with the width of the fingers, given by (Stern, 1960)

$$d = \left(\frac{\kappa_T \nu}{\alpha g \left| \frac{dT_0}{dz} - \frac{dT_{\text{ad}}}{dz} \right|} \right)^{1/4} = \left(\frac{\kappa_T \nu}{N_T^2} \right)^{1/4}, \quad (1.14)$$

where N_T is the local buoyancy frequency due to temperature stratification only. The non-dimensional units for length, time, and physical variables are then

$$[l] = d, \quad [t] = \frac{d^2}{\kappa_T}, \quad [u] = \frac{\kappa_T}{d}, \quad (1.15)$$

$$[T] = d \left(\frac{dT_0}{dz} - \frac{dT_{\text{ad}}}{dz} \right), \quad [C] = \frac{\alpha}{\beta} d \left(\frac{dT_0}{dz} - \frac{dT_{\text{ad}}}{dz} \right), \quad [B] = B_0, \quad (1.16)$$

where B_0 is the reference magnetic field strength. Carrying these through into the equations, and dropping the tildes, the final, non-dimensionalized system describing fingering convection in the

presence of magnetic fields is given by

$$\frac{\partial \hat{\mathbf{u}}}{\partial t} + \hat{\mathbf{u}} \cdot \nabla \hat{\mathbf{u}} = -\nabla \hat{p} + \text{Pr} \nabla^2 \hat{\mathbf{u}} + H_B (\nabla \times \hat{\mathbf{B}}) \times \hat{\mathbf{B}} + \text{Pr} (\hat{T} - \hat{C}) \hat{\mathbf{e}}_z, \quad (1.17)$$

$$\frac{\partial \hat{T}}{\partial t} + \hat{\mathbf{u}} \cdot \nabla \hat{T} + \hat{u}_z = \nabla^2 \hat{T}, \quad (1.18)$$

$$\frac{\partial \hat{C}}{\partial t} + \hat{\mathbf{u}} \cdot \nabla \hat{C} + \frac{\hat{u}_z}{R_0} = \tau \nabla^2 \hat{C}, \quad (1.19)$$

$$\frac{\partial \hat{\mathbf{B}}}{\partial t} = \nabla \times (\hat{\mathbf{u}} \times \hat{\mathbf{B}}) + D_B \nabla^2 \hat{\mathbf{B}}, \quad (1.20)$$

$$\nabla \cdot \hat{\mathbf{u}} = 0, \quad \nabla \cdot \hat{\mathbf{B}} = 0, \quad (1.21)$$

where from here onwards, hatted quantities denote non-dimensional ones and time and space variables have implicitly been made non-dimensional as well. In Eq. (1.17), $\hat{\mathbf{e}}_z$ denotes the unit vector in the z direction.

The non-dimensional parameters controlling the system are the Prandtl number Pr , the compositional and magnetic diffusivity ratios τ and D_B , respectively, the density ratio R_0 , and the Lorentz force coefficient H_B :

$$\text{Pr} = \frac{\nu}{\kappa_T}, \quad \tau = \frac{\kappa_C}{\kappa_T}, \quad R_0 = \frac{\alpha \left| \frac{dT_0}{dz} - \frac{dT_{\text{ad}}}{dz} \right|}{\beta \frac{dC_0}{dz}}, \quad (1.22)$$

$$H_B = \frac{B_0^2 d^2}{\rho_m \mu_0 \kappa_T^2}, \quad D_B = \frac{\eta}{\kappa_T}. \quad (1.23)$$

The Prandtl number Pr is of order one or larger in many geophysical scenarios (e.g. the very well-studied oceanic thermohaline convection, see Radko, 2013), but very small in stellar environments or liquid metals in planetary interiors (see Garaud, 2018, for an in-depth review). The ratios τ and R_0 parameterize the relative strength of diffusivities and effective stratification, respectively, between the thermal and compositional fields (R_0 is commonly referred to as the “density ratio”). From a linear stability analysis of pure fingering convection without magnetic fields (e.g., Baines and Gill, 1969), it is found that fingering convection occurs for $1 < R_0 < \tau^{-1}$ (Stern, 1960). The new parameters in Eqs. (1.23) parameterize the behavior of the magnetic field and its effect on fluid motion. The ratio D_B is simply the magnetic analogue to Pr and τ , and it is also small

in stellar environments and planetary interiors (although somewhat larger than Pr). The coefficient of the Lorentz force H_B is the squared ratio of the Alfvén velocity to the characteristic velocity. Because it depends on B_0^2 , it is thus the available “control parameter” that sets the strength of the background magnetic field. In both the analytical work and the numerical simulations that follow, we will vary this parameter with the goal of testing a variety of field strengths. We now briefly discuss what ranges of H_B values we might expect in stellar fingering convection.

The typical values of B_0 that are likely to occur in stellar interiors can vary widely both within a given star and between different stars, depending on the stellar region under consideration. The same is true for the local conditions of the fluid (and thus the values of the other physical parameters). For example, fingering convection occurs in MS and RGB stars at the base of the convective zone, while in WD stars it would occur at the surface following accretion of planets or debris. We provide order-of-magnitude estimates of ν , κ_T , ρ_m , and d in Table 1.1, for the regions of MS stars, RGB stars, and WD stars where fingering convection could occur. Based on these parameters, we can compute order-of-magnitude prefactors for H_B for these three scenarios, getting

$$H_B^{\text{MS}} \simeq \frac{1}{4\pi} \left(\frac{B_0}{100} \right)^2 \left(\frac{0.1}{\rho_m} \right)^2 \left(\frac{d}{10^4} \right)^2 \left(\frac{10^7}{\kappa_T} \right)^2 = 10^{-2} \left(\frac{B_0}{100} \right)^2, \quad (1.24)$$

$$H_B^{\text{RGB}} \simeq \frac{1}{4\pi} \left(\frac{B_0}{100} \right)^2 \left(\frac{1}{\rho_m} \right)^2 \left(\frac{d}{10^4} \right)^2 \left(\frac{10^9}{\kappa_T} \right)^2 = 10^{-7} \left(\frac{B_0}{100} \right)^2, \quad (1.25)$$

$$H_B^{\text{WD}} \simeq \frac{1}{4\pi} \left(\frac{B_0}{100} \right)^2 \left(\frac{1}{\rho_m} \right)^2 \left(\frac{d}{10} \right)^2 \left(\frac{10^4}{\kappa_T} \right)^2 = 10^{-3} \left(\frac{B_0}{100} \right)^2, \quad (1.26)$$

where all quantities in brackets are in cgs units. Clearly, since κ_T is so large in all stellar environments, we can expect that in general, H_B will be less than 1 as long as field strengths are limited to a few thousand Gauss. It is also likely that in some scenarios, such as in RGB stars, $H_B \ll 1$, which we might naively assume would mean that the effects of the background magnetic field are marginal. However, based on our numerical simulations and our analytical model, we will show in Section 5 that even for situations where H_B is small, the effects of background magnetic fields can be significant nonetheless.

Star type	κ_T	ν	ρ_m	$d = \left(\frac{\kappa_T \nu}{N_T^2}\right)^{1/4}$
Main Sequence	10^7	10	0.1	$10^{3.5} - 10^4$
Red Giant Branch	10^9	100	$100 - 0.1$	$10^{3.5} - 10^{4.5}$
White Dwarf	$10^2 - 10^6$	$10 - 100$	$10 - 0.1$	$10^{0.5} - 10^{1.5}$

Table 1.1: Order-of-magnitude estimates for various governing parameters within the expected fingering convection regions of Main Sequence stars, Red Giant Branch stars, and White Dwarfs. The ranges represent values from the lower radius to the upper radius of the fingering region. All units are in cgs.

2 Numerical tool: PADDIM

The system describing fingering convection in the presence of magnetic fields (Eqs. 1.17 - 1.21) is inherently nonlinear and is thus difficult to study using just theoretical methods, so developing a numerical code was paramount to this project. To this end, I developed the **PADDIM** code, a high-performance pseudo-spectral magnetohydrodynamics (MHD) code that numerically solves the double-diffusive MHD equations over a triply-periodic 3D domain (or doubly-periodic 2D domain). **PADDIM** is an MHD extension of the **PADDI** code (Traxler et al., 2011; Stellmach et al., 2011), which was originally developed to study pure double-diffusive convection. **PADDI** has been used in many successful studies and various versions have been written, including recent versions that add the effects of rotation to the mathematical model (Moll and Garaud, 2017; Sengupta and Garaud, 2018). As the original **PADDI** code already contains the basic infrastructure necessary for simulating double-diffusive convection in ordinary fluids, adding the effects of magnetic fields was simply a means of adjusting the mathematical model and modifying the I/O to accommodate the additional parameters and data associated with magnetic fields. In this section, I describe the general design of **PADDIM** and provide a few tests which I ran to verify its correctness.

2.1 PADDIM design overview

2.1.1 Physical model

The physical system modeled in PADDIM is that of incompressible MHD, under the Boussinesq approximation, along with evolution equations for the thermal and compositional fields:

$$\frac{\partial \mathbf{u}}{\partial t} + (\mathbf{u} \cdot \nabla) \mathbf{u} = -\nabla p + D_u \nabla^2 \mathbf{u} + H_B [(\nabla \times \mathbf{B}) \times \mathbf{B}] + (B_T T - B_C C) \hat{\mathbf{e}}_z, \quad (2.1)$$

$$\frac{\partial T}{\partial t} + (\mathbf{u} \cdot \nabla) T + S_T (\hat{\mathbf{e}}_z \cdot \mathbf{u}) = D_T \nabla^2 T, \quad (2.2)$$

$$\frac{\partial C}{\partial t} + (\mathbf{u} \cdot \nabla) C + S_C (\hat{\mathbf{e}}_z \cdot \mathbf{u}) = D_C \nabla^2 C, \quad (2.3)$$

$$\frac{\partial \mathbf{B}}{\partial t} = \nabla \times (\mathbf{u} \times \mathbf{B}) + D_B \nabla^2 \mathbf{B}, \quad (2.4)$$

$$\nabla \cdot \mathbf{u} = 0, \quad \nabla \cdot \mathbf{B} = 0. \quad (2.5)$$

The meanings of all these parameters are given in Table 2.1. These equations are effectively identical to those of the non-dimensionalized fingering convection system in Eqs. (1.17) - (1.21), with the only substantial difference being in how the non-dimensional coefficients in front of various terms have been named. This was done to simplify the code and allow maximum flexibility regarding non-dimensionalizations besides the standard fingering convection one chosen in Eqs. (1.17) - (1.21).

The domain Ω over which Eqs. (2.1) - (2.5) are modeled is a triply periodic box defined by

$$\Omega = \begin{cases} [0, \Gamma_x] \times [0, \Gamma_y] \times [0, \Gamma_z], & \text{for the 3D case} \\ [0, \Gamma_x] \times [0, \Gamma_z], & \text{for the 2D case} \end{cases}$$

where Γ_x , Γ_y , and Γ_z give the size of the box in each dimension. The initial conditions $\mathbf{u}(\mathbf{x}, 0)$, $\mathbf{B}(\mathbf{x}, 0)$, $T(\mathbf{x}, 0)$, $C(\mathbf{x}, 0)$ are specified by the user. This physical model is representative of a homogeneous incompressible flow, where the temperature and compositional fields (which may or may not be stratified) provide a source of buoyancy. The user may drop the temperature and compositional fields from the equations by leaving out some compiler flags, in which case the base physical model would simply be that of incompressible MHD with no body forces.

Symbol	Description
\mathbf{u}	Fluid velocity
\mathbf{B}	Magnetic field
T	Temperature field
C	Chemical/Compositional field
p	Fluid pressure
D_u	Velocity diffusion coefficient
H_B	Lorentz force coefficient
B_T	Thermal buoyancy coefficient
B_C	Compositional buoyancy coefficient
D_T	Thermal diffusion coefficient
S_T	Thermal stratification coefficient
D_C	Compositional diffusion coefficient
S_C	Compositional stratification coefficient
D_B	Magnetic diffusion coefficient

Table 2.1: The meaning of the parameters in Eqs. (2.1) - (2.5). The coefficients of various terms (e.g. D_u , H_B , etc) are written as such to support many different possible non-dimensionalizations.

2.1.2 Numerical scheme

PADDIM uses a pseudo-spectral scheme to numerically solve Eqs. (2.1) - (2.5), which gives it the advantage of higher accuracy at lower computational cost compared to simpler finite difference methods. The approach is similar to the classic scheme presented in Patterson and Orszag (1971) and Orszag and Patterson (1972). The primitive variables $(\mathbf{u}, \mathbf{B}, T, C)$ are approximated by their Fourier series representations truncated at maximum wave numbers in each of the x , y , and z directions, and their spectral space representations $(\tilde{\mathbf{u}}, \tilde{\mathbf{B}}, \tilde{T}, \tilde{C})$ are advanced in time according to the ordinary differential equations (ODEs) that arise when transforming Eqs. (2.1) - (2.5). Doing so transforms the spatial linear differential operators into vector multiplications by the wave vector \mathbf{k} , which can be solved exactly up to machine accuracy. The nonlinear terms are calculated in physical space and then transformed back into spectral space in order to advance the ODEs. An outline of a procedure similar to this is given in §3.3.1 of Canuto et al. (2007). In PADDIM, all Fourier transforms are performed using a parallelized fast Fourier transform (FFT) algorithm that makes use of the FFTW library to optimize performance.

The treatment of the velocity field employs a few simplifying tricks to make the code more

stable and convenient to implement, which are worth mentioning. First, using the identity

$$(\mathbf{u} \cdot \nabla) \mathbf{u} = (\nabla \times \mathbf{u}) \times \mathbf{u} + \frac{1}{2} \nabla (\mathbf{u} \cdot \mathbf{u}),$$

we can rewrite Eq. 2.1 as

$$\frac{\partial \mathbf{u}}{\partial t} + (\nabla \times \mathbf{u}) \times \mathbf{u} = -\nabla q + D_u \nabla^2 \mathbf{u} + \mathbf{F}, \quad (2.6)$$

where \mathbf{F} represents the body force terms all grouped together and q is the dynamic pressure given by

$$q = p + \frac{1}{2} (\mathbf{u} \cdot \mathbf{u}).$$

When transformed into spectral space, with the diffusion term treated implicitly and the body force and advection terms treated explicitly, Eq. 2.6 yields an ODE for each wave mode \mathbf{k} given by

$$\left(\frac{d}{dt} + D_u |\mathbf{k}|^2 \right) \tilde{\mathbf{u}}_{\mathbf{k}} = -i \mathbf{k} \tilde{q}_{\mathbf{k}} + \tilde{\mathbf{F}}_{\mathbf{k}} - \tilde{\mathbf{c}}_{\mathbf{k}}, \quad (2.7)$$

where $\tilde{\mathbf{c}}_{\mathbf{k}}$ corresponds to the Fourier transform of the $(\nabla \times \mathbf{u}) \times \mathbf{u}$ term. This is the ODE solved by PADDIM to advance the velocity field in time. Besides improving stability, another advantage of advancing \mathbf{u} via the form in Eq. 2.6 is that PADDIM already has the vorticity $\boldsymbol{\omega} = \nabla \times \mathbf{u}$ on hand, calculated exactly in spectral space and then transformed into physical space, as an output variable.

A major convenience provided by the fact that PADDIM is a pseudo-spectral code is that the divergence-free condition, $\nabla \cdot \mathbf{B} = 0$, is adequately satisfied without extra computation. In finite difference codes, even when starting from an initial state satisfying $\nabla \cdot \mathbf{B} = 0$, the finite-differencing approximation of spatial derivatives introduces nonzero errors that can accumulate as the simulation progresses. If the divergence-free condition is not satisfied, it is possible to have unphysical fluid transport orthogonal to magnetic field lines, among a host of other issues (Brackbill and Barnes, 1980). In such situations, much care has to be taken to minimize or eliminate this error via some sort of “divergence-cleaning” or staggered mesh approach. An overview of and comparison between various approaches is given in Balsara and Kim (2004). In PADDIM, the divergence-cleaning headache is avoided, since $\nabla \cdot \mathbf{B} = 0$ can be satisfied up to machine accuracy in spectral space because the

divergence operator simplifies to a dot product with the wave vector \mathbf{k} . There are non-zero errors introduced when transforming back into physical space, but these are negligible because they do not accumulate as the simulation advances – indeed, in production runs, calculating $\nabla \cdot \mathbf{B}$ at each time step showed that it never grew past machine accuracy.

The chief time-stepping scheme in PADDIM is the third-order Adams-Bashforth/Backward-Differentiation-Formula (AB/BDF3) method. This is supplemented at start-up using a second order Runge-Kutta/Crank-Nicholson (RK/CN2) scheme. The AB/BDF3 scheme is a multi-step method of the form

$$\frac{1}{\Delta t} \sum_{j=0}^k a_j u^{n+1-j} = \sum_{j=0}^{k-1} H(u^{n-j}), \quad (2.8)$$

where u^n is the solution at timestep n , H is the operator on the RHS in the equation $\partial_t u = H(u)$, Δt is the time step size, and a_j, b_j are coefficients. Ordinarily, the a_j and b_j in Eq. 2.8 are fixed values, but since the time step must change in PADDIM according to the Courant-Friedrichs-Lewy (CFL) condition, these coefficients must be expressed in terms of the sizes of previous time steps. Through a straightforward but laborious Taylor expansion of the local truncation error, the expressions relating these coefficients to the ratios of current and previous time steps can be computed and are given in §4.5.1 of Peyret (2002).

2.2 Verification & Testing

There are three major components of the system (2.1) - (2.5) in PADDIM which needed to be tested in order to validate the new physical model. The first two are magnetic diffusion and induction of magnetic field through fluid motions, which arise from the induction equation (Eq. 2.4). The third is the effect of the Lorentz force on the velocity, which is the $(\nabla \times \mathbf{B}) \times \mathbf{B}$ term in Eq. (2.1). Each of these were tested in succession by exciting eigenmodes of a simple test problem in order to verify the accuracy of the numerical solution.

2.2.1 Magnetic diffusion

The test for magnetic diffusion was the simplest of the three, as it depends only on the magnetic field and thus can be tested by ignoring the velocity field entirely. Setting the induction term in Eq. (2.4) to zero, we have

$$\frac{\partial \mathbf{B}}{\partial t} = D_B \nabla^2 \mathbf{B}.$$

The eigenfunctions of the above operator are sines and cosines, which naturally satisfy the periodic boundary conditions, and since PADDIM saves profiles of simulation variables along the z -direction, the test problem was set up as

$$\begin{aligned} \frac{\partial B_x}{\partial t} &= D_B \frac{\partial^2 B_x}{\partial z^2}, \\ B_x(x, y, z, t = 0) &= B_0 \sin\left(\frac{2\pi z}{\Gamma_z}\right), \\ B_y(x, y, z, t) &= B_z(x, y, z, t) = 0. \end{aligned}$$

The analytical solution to this problem is

$$B_x(x, y, z, t) = B_0 e^{-[D_B(2\pi/\Gamma_z)^2]t} \sin\left(\frac{2\pi z}{\Gamma_z}\right).$$

The numerical solution matched the analytical solution up to machine accuracy, with a mean difference of 2.3×10^{-18} . Figure 2.1 shows a plot of the numerical solution.

2.2.2 Velocity-induced magnetic field

Testing the “induction” part of the induction equation was done with a simple kinematic model (where the velocity field drives induction of magnetic field via Eq. (2.4) but there is no feedback on the velocity field via the Lorentz force). To get a stable, non-turbulent flow field, the thermal and compositional fields were ignored and a forcing term was added to the non-dimensionalized momentum equation, giving

$$\frac{\partial \mathbf{u}}{\partial t} + (\mathbf{u} \cdot \nabla) \mathbf{u} = -\nabla p + \frac{1}{\text{Re}} \nabla^2 \mathbf{u} + F_0 \sin\left(\frac{2\pi z}{\Gamma_z}\right) \hat{\mathbf{e}}_x. \quad (2.9)$$

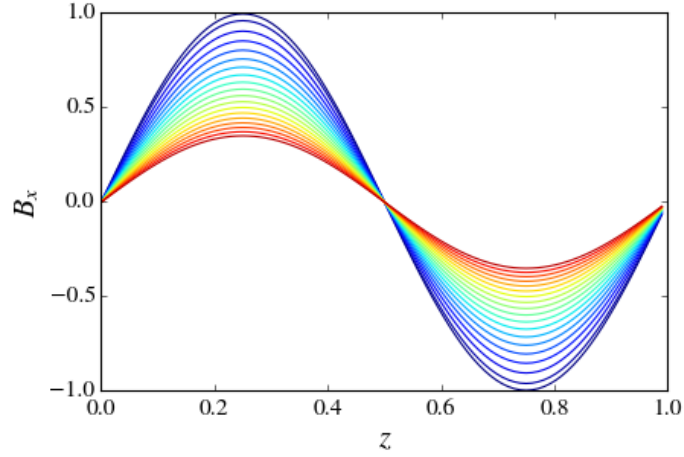


Figure 2.1: The numerical results for the vertical profile of the x -component of the magnetic field at several time steps during the magnetic diffusion test. The profile of each time step plotted is colored according to simulation time, with blue corresponding to $t = 0$ and red corresponding to the end of the simulation.

The laminar solution to Eq. 2.9 can be found by imposing a balance between the diffusion and forcing terms, which in the x -direction (the direction of forcing) yields

$$\mathbf{u}_L(z) = \left(\frac{F_0 \Gamma_z^2 \text{Re}}{4\pi^2} \right) \sin\left(\frac{2\pi z}{\Gamma_z}\right) \hat{\mathbf{e}}_x. \quad (2.10)$$

Choosing a simple non-dimensionalization where $\Gamma_z = \max |u_L| = \text{Re} = 1$ (thus $F_0 = 4\pi^2$), we can solve the induction equation with this prescribed $\mathbf{u} = (u_L, 0, 0)$. If B_y and B_z are initially zero in this setup, they will remain as such. Thus, with $B_z(x, y, z, t = 0) = B_0$, the induction equation with no diffusion reduces to

$$\frac{\partial B_x}{\partial t} = \frac{\partial}{\partial y}(u_x B_y - u_y B_x) - \frac{\partial}{\partial z}(u_z B_x - u_x B_z) = \frac{\partial}{\partial z}(u_x B_z) = B_0 \frac{\partial u_L}{\partial z} = B_0 2\pi \cos(2\pi z), \quad (2.11)$$

which has the solution $B_x = B_0 2\pi t \cos(2\pi z)$. Then, for the full problem with diffusion, we adopt an ansatz where B_x is of the form $B_x = B_{x0}(t) \cos(2\pi z)$, which gives the ODE

$$\frac{dB_{x0}}{dt} = 2\pi B_0 - D_B(4\pi^2)B_{x0}. \quad (2.12)$$

The solution to Eq. (2.12) is

$$B_{x0}(t) = \frac{B_0}{2\pi D_B} (1 - e^{-D_B 4\pi^2 t}), \quad (2.13)$$

which determines the envelope of the analytical solution for B_x in this laminar test problem. Running PADDIM initialized with the laminar problem and the chosen non-dimensionalization yielded results that matched this analytical solution up to machine accuracy. Figure 2.2 shows the numerical results for B_x growing from zero according to Eq. 2.13 as it is induced by the laminar flow. The mean magnitude of the difference between the numerical results and the analytical solution was 1.06×10^{-16} .

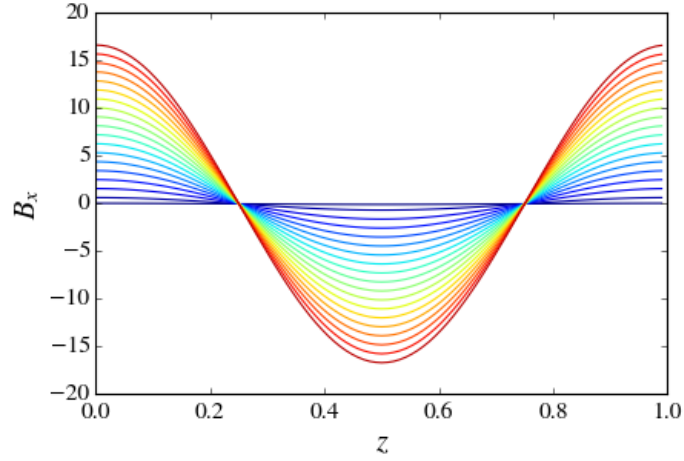


Figure 2.2: The numerical results for the vertical profile of the x -component of the magnetic field at several time steps during the Laminar flow kinematic dynamo test. The profile of each time step plotted is colored according to simulation time, with blue corresponding to $t = 0$ and red corresponding to the end of the simulation.

2.2.3 Lorentz force

To test the full MHD “feedback loop”, where \mathbf{u} affects \mathbf{B} via the induction equation and \mathbf{B} affects \mathbf{u} via the Lorentz force, a test problem that excited shear Alfvén waves was set up. Shear Alfvén waves propagate along the direction of the background field \mathbf{B}_0 , with wave speed

$$v_A = \frac{\omega}{k} = \frac{B_0}{\sqrt{\mu_0 \rho_m}}.$$

We consider a magnetic field $\mathbf{B} = \mathbf{B}_0 + \mathbf{b}$, where the perturbations \mathbf{b} are given by $\mathbf{b} = \|\mathbf{b}\|e^{i\mathbf{k}\cdot\mathbf{x}}$ where $\|\mathbf{b}\| \ll \|\mathbf{B}_0\|$ and $\mathbf{k} \parallel \mathbf{B}_0$. Carrying this into the equations, then linearizing (and non-

dimensionalizing) the system yields

$$\frac{\partial \mathbf{b}}{\partial t} = \nabla \times (\mathbf{u} \times \mathbf{B}_0) + \frac{1}{R_m} \nabla^2 \mathbf{b}, \quad (2.14)$$

$$\frac{\partial \mathbf{u}}{\partial t} = -\nabla p + H_B((\nabla \times \mathbf{b}) \times \mathbf{B}_0) + \frac{1}{Re} \nabla^2 \mathbf{u}, \quad (2.15)$$

where R_m is the magnetic Reynolds number. If we align \mathbf{B}_0 along the z direction and take \mathbf{b} to have no x component (without loss of generality), we get a wave equation in b_y and u_y . Then, choosing initial conditions such that $u_y = \frac{\partial b_y}{\partial t} = 0$, we get a system where the waves in the velocity and magnetic fields should have the same wave number and frequency, with the u_y waves phase-shifted by a quarter-period. Taking the perturbations as 1% of the magnitude of the background magnetic field (which has magnitude 1 by the non-dimensionalization), these linearized solutions are given by

$$b_y(\mathbf{x}, t) = 0.01 \sin(10\pi z) \cos(10\pi \sqrt{H_B} t) \quad (2.16)$$

$$u_y(\mathbf{x}, t) = 0.01 \sqrt{H_B} \cos(10\pi z) \sin(10\pi \sqrt{H_B} t) \quad (2.17)$$

Running this test problem in PADDIM with $H_B = 0.01$ produced the expected behavior. Figure 2.3 shows various temporal snapshots of the analytical linearized solutions Eqs. (2.16)-(2.17) as well as the fully nonlinear numerical solutions, as a vertical profile along the $x = y = 0$ line. The mean relative difference between the two solutions was about 1.4% for both the magnetic and velocity fields, which is reasonable considering that Eqs. (2.16)-(2.17) are just linear approximations of the actual physical behavior and do not account for diffusion. The waves clearly have the same wave number and frequency, with the appropriate quarter-period phase shift.

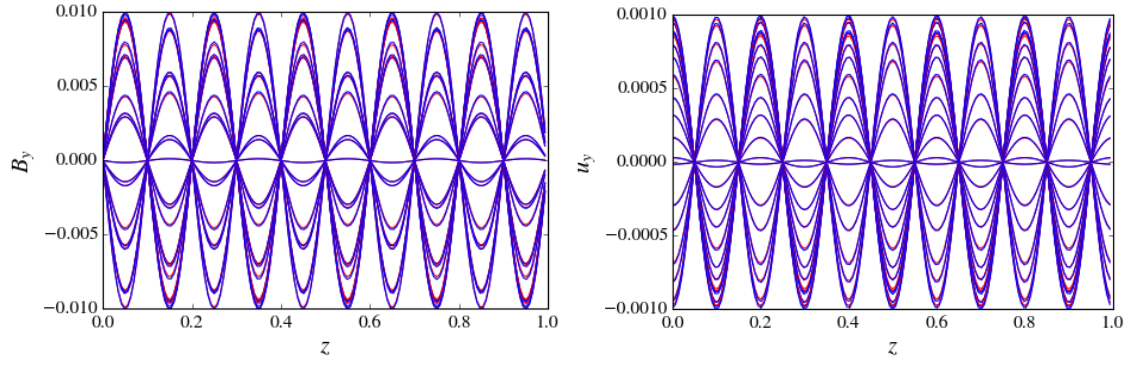


Figure 2.3: The numerical results (red) and the analytical linearized solutions (blue) for the vertical profiles of the y -component of the magnetic field (left) and the velocity field (right) at several time steps during the Alfvén wave test.

3 Linear stability analysis

A standard first step taken in studying fluid instabilities is a linear stability analysis, which simplifies the governing equations by removing nonlinearities and explicitly models fluid behavior in terms of the growth of small perturbations from an initial state. In the interest of studying fingering convection in the presence of a background magnetic field (Eqs. 1.17 - 1.21), we will assume a constant background field of unit intensity along the ξ direction to which we add a small perturbation $\hat{\mathbf{b}}$ such that

$$\hat{\mathbf{B}} = \hat{\mathbf{e}}_\xi + \hat{\mathbf{b}}, \quad (3.1)$$

where $\hat{\mathbf{e}}_\xi$ is the unit vector in the ξ direction. Then, as in the analysis for ordinary fingering convection (e.g., Baines and Gill, 1969), we take small perturbations of the form

$$\hat{\mathbf{u}} = \tilde{\mathbf{u}} \exp(\hat{\lambda}t + i(\hat{\mathbf{k}} \cdot \mathbf{x})), \quad (3.2)$$

$$\hat{T} = \tilde{T} \exp(\hat{\lambda}t + i(\hat{\mathbf{k}} \cdot \mathbf{x})), \quad (3.3)$$

$$\hat{C} = \tilde{C} \exp(\hat{\lambda}t + i(\hat{\mathbf{k}} \cdot \mathbf{x})), \quad (3.4)$$

$$\hat{\mathbf{b}} = \tilde{\mathbf{b}} \exp(\hat{\lambda}t + i(\hat{\mathbf{k}} \cdot \mathbf{x})), \quad (3.5)$$

where $\hat{\lambda}$ is the growth rate of each mode, $\hat{\mathbf{k}} = (\hat{k}_x, \hat{k}_y, \hat{k}_z)$ is the wave vector, $\mathbf{x} = (x, y, z)$, and $\tilde{\mathbf{u}}$, \tilde{T} , \tilde{C} , and $\tilde{\mathbf{b}}$ are fixed.

Substituting these perturbations into Eqs. (1.17) - (1.21) transforms the spatial differential operators into vector multiplication operations with $i\hat{\mathbf{k}}$, and the temporal derivatives into multiplications by the growth rate $\hat{\lambda}$. The divergence-free conditions in Eq. (1.17) thus become $i\hat{\mathbf{k}} \cdot \hat{\mathbf{u}} = 0$ and

$i\hat{\mathbf{k}} \cdot \hat{\mathbf{b}} = 0$. To linearize the system, assume all terms which are nonlinear in the perturbations (the advective terms and the pure-perturbative component of the Lorentz force) are sufficiently small such that they may be removed. The governing equations are then reduced to the simplified set of algebraic equations

$$(\hat{\lambda} + \text{Pr}\hat{k}^2)\tilde{\mathbf{u}} = -i\hat{\mathbf{k}}\hat{p} + \text{Pr}(\hat{T} - \hat{C})\hat{\mathbf{e}}_z + H_B[(i\hat{\mathbf{k}} \times \tilde{\mathbf{b}}) \times \hat{\mathbf{e}}_\xi], \quad (3.6)$$

$$(\hat{\lambda} + \hat{k}^2)\tilde{T} + \tilde{u}_z = 0, \quad (3.7)$$

$$(\hat{\lambda} + \tau\hat{k}^2)\tilde{C} + \frac{\tilde{u}_z}{R_0} = 0, \quad (3.8)$$

$$(\hat{\lambda} + D_B\hat{k}^2)\tilde{\mathbf{b}} = i\hat{k}_\xi\tilde{\mathbf{u}}, \quad (3.9)$$

where $\hat{k}_\xi = \hat{\mathbf{k}} \cdot \hat{\mathbf{e}}_\xi$ and $\hat{k}^2 = k_x^2 + k_y^2 + k_z^2$. The relations in Eqs. (3.6) - (3.9) can be used to eliminate \tilde{T} , \tilde{C} , and $\tilde{\mathbf{b}}$, which after some simplification gives

$$(\hat{\lambda} + \text{Pr}\hat{k}^2)\tilde{\mathbf{u}} = -i\hat{\mathbf{k}}\hat{p} + \text{Pr}\tilde{u}_z\left(\frac{1}{R_0(\hat{\lambda} + \tau\hat{k}^2)} - \frac{1}{(\hat{\lambda} + \hat{k}^2)}\right)\hat{\mathbf{e}}_z - \frac{\hat{k}_\xi H_B}{(\hat{\lambda} + D_B\hat{k}^2)}(\hat{k}_\xi\tilde{\mathbf{u}} - \tilde{u}_\xi\hat{\mathbf{k}}), \quad (3.10)$$

where $\tilde{u}_\xi = \tilde{\mathbf{u}} \cdot \hat{\mathbf{e}}_\xi$. To eliminate pressure, we take the dot product of both sides with $\hat{\mathbf{k}}$ and impose the $\hat{\mathbf{k}} \cdot \hat{\mathbf{u}} = 0$ constraint to get

$$i\hat{p} = \frac{\text{Pr}\tilde{u}_z\hat{k}_z}{\hat{k}^2}\left(\frac{1}{R_0(\hat{\lambda} + \tau\hat{k}^2)} - \frac{1}{(\hat{\lambda} + \hat{k}^2)}\right) + \frac{\hat{k}_\xi\tilde{u}_\xi H_B}{(\hat{\lambda} + D_B\hat{k}^2)}. \quad (3.11)$$

Substituting Eq. (3.11) back into Eq. (3.10) leads to a convenient cancellation of the Lorentz force term along the $\hat{\mathbf{k}}$ direction, which gives the relation

$$\left(\hat{\lambda} + \text{Pr}\hat{k}^2 + \frac{\hat{k}_\xi^2 H_B}{\hat{\lambda} + D_B\hat{k}^2}\right)\tilde{\mathbf{u}} = \text{Pr}\tilde{u}_z\left(\frac{1}{R_0(\hat{\lambda} + \tau\hat{k}^2)} - \frac{1}{(\hat{\lambda} + \hat{k}^2)}\right)\left(-\frac{\hat{k}_z}{\hat{k}^2}\hat{\mathbf{k}} + \hat{\mathbf{e}}_z\right). \quad (3.12)$$

Taking the z -component, we get

$$\left(\hat{\lambda} + \text{Pr}\hat{k}^2 + \frac{\hat{k}_\xi^2 H_B}{\hat{\lambda} + D_B\hat{k}^2}\right) = \text{Pr}\left(\frac{1}{R_0(\hat{\lambda} + \tau\hat{k}^2)} - \frac{1}{(\hat{\lambda} + \hat{k}^2)}\right)\left(\frac{\hat{k}_H^2}{\hat{k}^2}\right), \quad (3.13)$$

where \hat{k}_H^2 is the square of the horizontal wave number, defined by $\hat{k}_H^2 = \hat{k}_x^2 + \hat{k}_y^2$. Here we can immediately see that setting $H_B = 0$ reproduces the relation that arose from the hydrodynamic case. More interestingly, the same is true for $\hat{k}_\xi = 0$ which corresponds to perturbations for which

$\hat{\mathbf{k}}$ is perpendicular to the magnetic field. This reveals that no matter the value of H_B or D_B , the growth rate of modes with $\hat{k}_\xi = 0$ will remain the same as in the hydrodynamic limit. Furthermore, since we can always pick both $\hat{k}_\xi = 0$ and $\hat{k}_z = 0$, the fastest-growing modes of magnetic fingering convection (the $k_z = 0$ “elevator modes”, see Radko, 2013) will grow at the same rate as in the hydrodynamic case.

In their stability analysis of magnetized fingering convection (which differed in a number of ways from this one), Charbonnel and Zahn (2007b) developed a relation for the growth rate of the fingers which depended on $\hat{\mathbf{k}} \cdot \hat{\mathbf{B}}_0$, where $\hat{\mathbf{B}}_0$ represents the background field. They interpreted their result as showing that the magnetic field could stabilize the system to fingering convection, but they failed to note that setting $\hat{\mathbf{k}} \cdot \hat{\mathbf{B}}_0 = 0$ implies that the growth rate is unaffected by the presence of the field when $\hat{\mathbf{k}}$ is perpendicular to $\hat{\mathbf{B}}_0$.

3.1 Region of instability and fastest-growing modes

We can rearrange Eq. (3.13) to yield a quartic polynomial in $\hat{\lambda}$, of the form

$$\hat{\lambda}^4 + \alpha_3 \hat{\lambda}^3 + \alpha_2 \hat{\lambda}^2 + \alpha_1 \hat{\lambda} + \alpha_0 = 0, \quad (3.14)$$

where the coefficients α_i are given by

$$\alpha_3 = \hat{k}^2(\text{Pr} + D_B + \tau + 1), \quad (3.15)$$

$$\alpha_2 = \hat{k}_\xi^2 H_B + \hat{k}^4 D_B \text{Pr} + \hat{k}^4 (\text{Pr} + D_B)(1 + \tau) + \hat{k}^4 \tau - \text{Pr} \frac{\hat{k}_H^2}{\hat{k}^2} (R_0^{-1} - 1), \quad (3.16)$$

$$\alpha_1 = \hat{k}^2(1 + \tau)(\hat{k}^4 D_B \text{Pr} + \hat{k}_\xi^2 H_B) + \hat{k}^6 (\text{Pr} + D_B) \tau - \text{Pr} \hat{k}_H^2 (D_B (R_0^{-1} - 1) + (R_0^{-1} - \tau)), \quad (3.17)$$

$$\alpha_0 = \tau \hat{k}^4 (\hat{k}^4 D_B \text{Pr} + \hat{k}_\xi^2 H_B) - \text{Pr} \hat{k}_H^2 \hat{k}^2 D_B (R_0^{-1} - \tau). \quad (3.18)$$

For the system to be linearly unstable, there must be at least one root of Eq. (3.14) with positive real part. If all coefficients α_i are positive, then there are no such roots, according to the Routh-Hurwitz theorem. Thus, a necessary condition for instability is that at least one of the α_i must be negative. Since we need $R_0 > 1$ to prevent standard overturning convection, the necessary

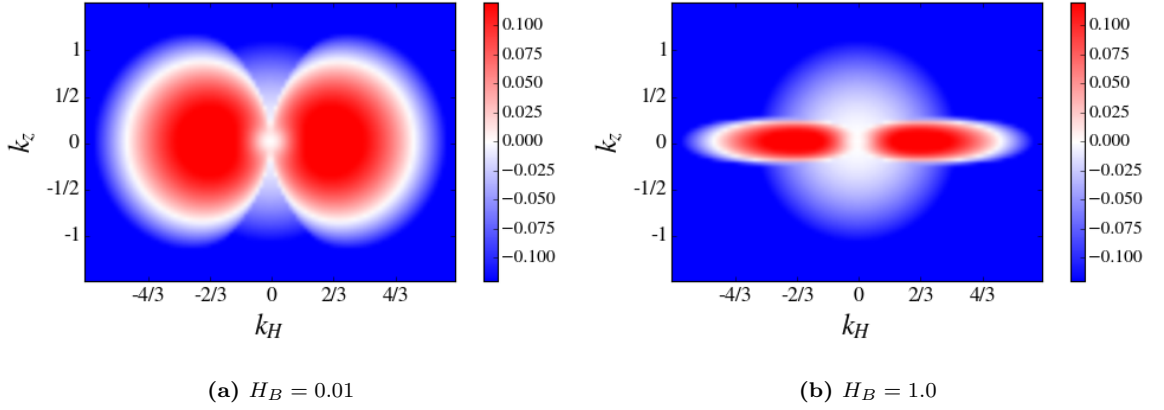


Figure 3.1: Maximum real part of all roots of the growth rate polynomial in Eq. (3.14) as a function of horizontal wave number \hat{k}_H and vertical wave number \hat{k}_z , for a background magnetic field along the z -direction with intensities corresponding to (a) $H_B = 0.01$ and (b) $H_B = 1$. The other parameters are $\text{Pr} = \tau = \text{D}_B = 0.1$, $R_0 = 1.45$ for both plots, and red colors indicate instability.

condition for instability to fingering convection in the presence of a background magnetic field is thus $1 < R_0 < \tau^{-1}$, which is the same condition found for the non-magnetic case (Stern, 1960).

The maximum growth rate for the instability (i.e., the maximal positive real part of the roots of Eq. 3.14) occurs for $\hat{k}_\xi = 0$. If the background magnetic field (\hat{e}_ξ) is aligned along the z direction, then the $\hat{k}_\xi = 0$ condition for the fastest growing modes is simply the $\hat{k}_z = 0$ condition for the elevator modes of the non-magnetic case. As the background magnetic field becomes increasingly horizontal, the fastest growing modes can still have $\hat{k}_z = 0$ (and are thus still elevator modes) but will also satisfy $\hat{k}_\xi = 0$. Increasing the strength of the background magnetic field, and thus H_B , effectively “squashes” the unstable region of $\hat{\mathbf{k}}$ -space by suppressing modes of larger \hat{k}_ξ .

A simple way of visualizing the unstable region of $\hat{\mathbf{k}}$ -space is to numerically solve the stability polynomial, or special cases of it, for a given set of parameters. This was done for $\text{Pr} = \tau = \text{D}_B = 0.1$, $R_0 = 1.45$, for a variety of inclinations and intensities of the background field. Figure 3.1 shows results for the case where the background magnetic field is in the vertical direction, as a function of vertical and horizontal wave number, for $H_B = 0.01$ and $H_B = 1.0$. The $H_B = 0.01$ case, representing a relatively weak background magnetic field, resembles the unstable region for the non-magnetic case. When the background magnetic field strength is increased to make $H_B = 1.0$,

the modes with higher $|\hat{k}_z|$ are suppressed and the unstable region in $\hat{\mathbf{k}}$ -space shrinks. These results resemble those of the stability region for rotating fingering convection in the case where the rotation axis is also aligned in the vertical direction (see Fig. 1 of Sengupta and Garaud, 2018).

If the background magnetic field is inclined from the z -axis by some angle θ , the region of $\hat{\mathbf{k}}$ -space unstable to fingering convection departs more noticeably from the non-magnetic case. Figure 3.2 shows surfaces of null stability for $\theta \in \{0, \pi/6, \pi/3, \pi/2\}$, with a background magnetic field strength corresponding to $H_B = 1.0$. This represents a relatively strong field, so the modes with higher \hat{k}_ξ are suppressed, making a disc-like structure that rotates along with the direction of the background field (note that in Fig. 3.2, the background magnetic field is chosen to have no component along the y -direction, without loss of generality). If $\theta = \pi/2$, then the background field is completely aligned with the x -direction and it suppresses modes with higher $|\hat{k}_x|$. Thus, the linear stability predicts that in this case, the “fingers” should be arranged into more sheet-like structures since their variation along the x -direction is significantly reduced.

3.2 Verification via DNS

The early-time behavior of the instability predicted by the linear stability analysis can be confirmed from some DNS results. To this end, several simulations were run with the parameters $\text{Pr} = \tau = \text{D}_B = 0.1$, $R_0 = 1.45$, and $H_B \in \{0.01, 0.1, 1, 10, 100\}$, for fields aligned in the z -direction as well as the x -direction (a detailed discussion of the DNS parameters used is given in the next section). All simulations are initialized with the fluid completely at rest, with a uniform magnetic field, and with randomly generated small-amplitude perturbations in the \hat{T} and \hat{C} fields. These small perturbations create a “source” spectrum of modes where the stable modes decay away but the unstable modes begin to grow via the fingering instability. An effect of this initialization not seen in non-magnetic fingering convection is that when the initial magnetic energy is large compared to the kinetic energy, the very small-scale perturbations seem to generate a group of Alfvén waves and secondary currents, which dissipate relatively quickly, but still generate some numerical noise

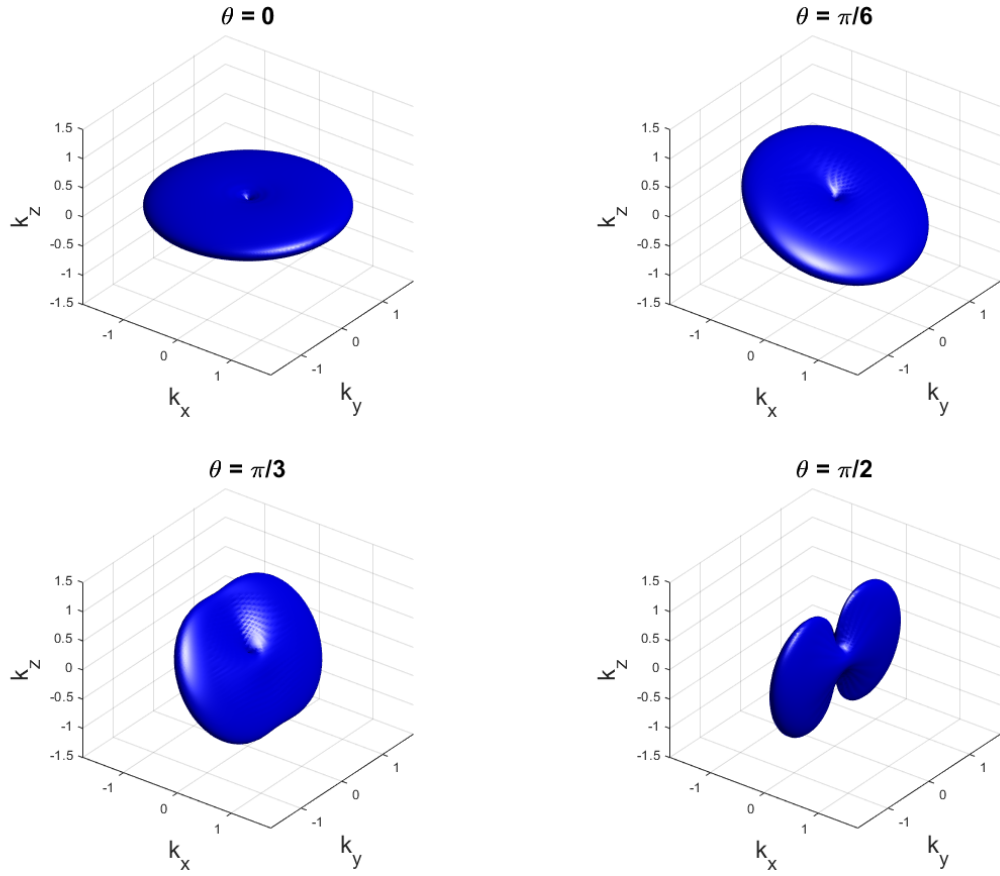


Figure 3.2: Surfaces of null stability for background magnetic field inclinations of $\theta \in \{0, \pi/6, \pi/3, \pi/2\}$ at $H_B = 1$. The background field is chosen, without loss of generality, to have no component along the y direction. Artificial lighting is included to render the bumps in the surface.

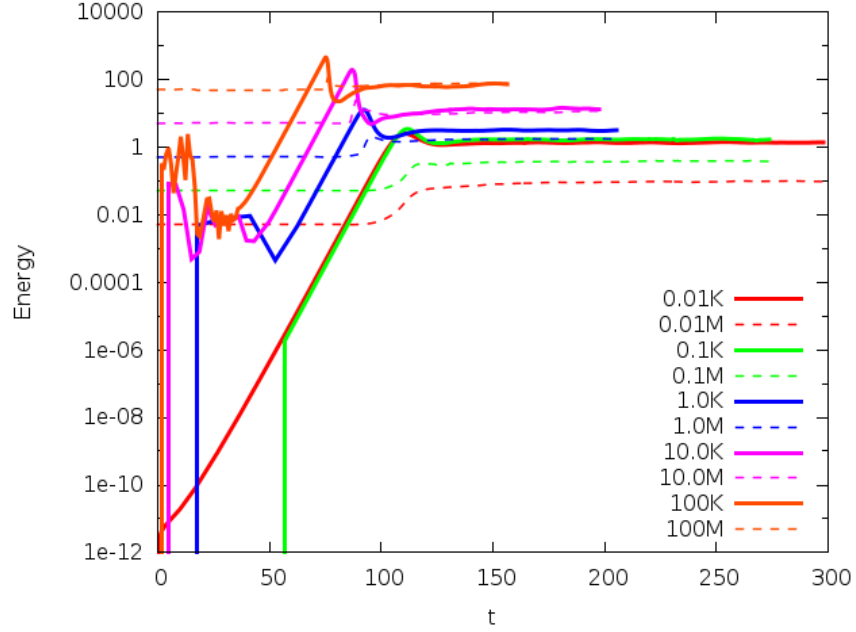


Figure 3.3: The kinetic (“K”, solid lines) and magnetic (“M”, dashed lines) energies as a function of time (in units of the thermal diffusion timescale) for simulations with the background magnetic field aligned along the z -direction. The background field strengths in each run correspond to $H_B = 0.01$ (red), $H_B = 0.1$ (green), $H_B = 1$ (blue), $H_B = 10$ (purple), and $H_B = 100$ (orange).

in the fluid velocity and kinetic energy at the beginning of the simulation. However, the noise is small relative to the saturation peak and post-saturation phases of the instability, and the ratio of magnetic energy to kinetic energy in the presence of the noise remains large (since the velocity perturbations are essentially “tapping into” the large background energy of the magnetic field). It dies off well before the saturation peak is reached, so it is deemed inconsequential.

Figure 3.3 shows the growth of the kinetic and magnetic energies over time for all simulations where the magnetic field is aligned with the z -axis. At early times, the numerical noise discussed above is visible for the cases with stronger background magnetic fields. However, once the noise dies off, it is clear to see that the instability grows at a constant exponential growth rate (straight-line on a semi-log plot) until reaching the saturation peak. Since the trajectories of the kinetic energy for all strengths of the background field ($0.01 \leq H_B \leq 100$) are roughly parallel during the growth phase, we can confirm our prediction that the growth rate of the fastest growing modes is unaffected by the magnetic field.

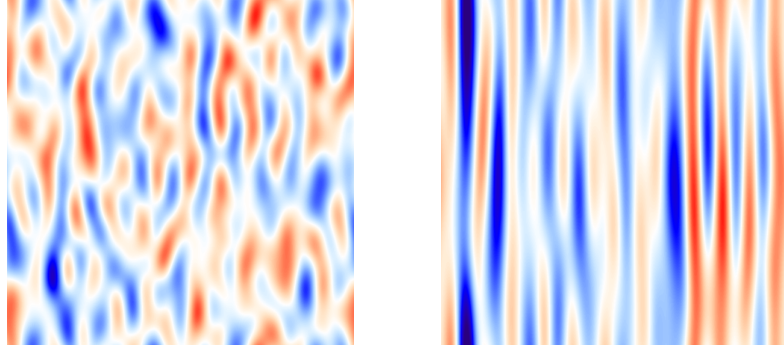


Figure 3.4: Two snapshots of the compositional perturbations in the x - z plane taken at early times in simulations with a vertical background magnetic field. The left panel shows a weak-field case, with $H_B = 0.01$, while the right panel shows how a stronger field, with $H_B = 1$, makes the finger structure more dominated by the $\hat{k}_z = 0$ “elevator modes”. Color scale runs from -0.036 (blue) to +0.036 (red) on the left, and from -1.20 (blue) to 1.20 (red) on the right, both in non-dimensional units.

For the case where the background field is aligned with the vertical axis, the fastest-growing modes are the $\hat{k}_z = 0$ “elevator modes”, and larger background magnetic field strengths will suppress the growth rate of modes with higher $|\hat{k}_z|$. Thus, modes with low (but non-zero) $|k_z|$ which grow in the presence of a weak field (or with no magnetic field) become stable as we increase the background field strength. Figure 3.4 shows this effect, with two snapshots of the compositional perturbation in the x - z plane taken at early times for simulations at $H_B = 0.01$ and $H_B = 1.0$. For the case where the background magnetic field is along a horizontal direction, taken here to be the x direction, the fastest growing modes have $\hat{k}_x = 0$, and larger background magnetic field strengths suppress the growth rate of modes with higher $|\hat{k}_x|$. Thus, the initial fingers in this case should become more invariant along the x -direction. Figure 3.5 shows such behavior, with two snapshots of the compositional perturbation in the x - y plane at early times in simulations of both the vertical and horizontal magnetic field cases.

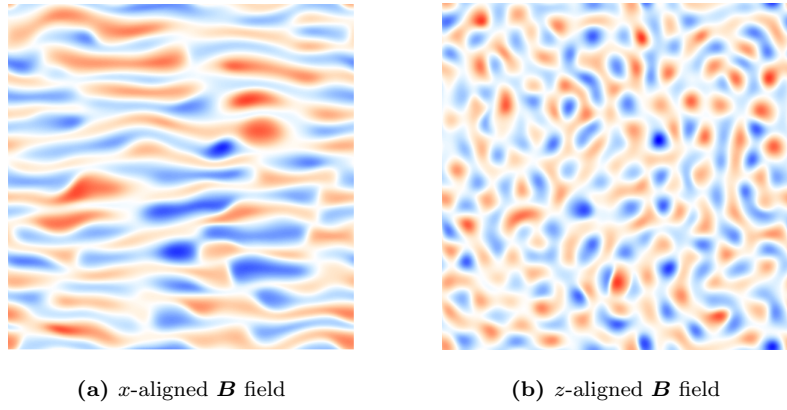


Figure 3.5: Two snapshots of the compositional field in the x - y plane taken at early times in a simulation with a horizontal background magnetic field (a) and a vertical background magnetic field (b). Color scale runs from -20 (blue) to +20 (red) in non-dimensional units.

4 Numerical Simulations

We now turn our attention to the full suite of numerical simulations, which are the primary component of this thesis, in order to study in depth the nonlinear saturation and post-saturation behavior of magnetized fingering convection. These simulations showcase a variety of orientations and strengths of the background magnetic field, but all share the same values for the “non-magnetic” parameters. In some runs with strong background fields, the domain size in the vertical direction is extended in order to sufficiently minimize effects incurred by the size of the domain and its periodic boundary conditions (similar steps were taken in some of the rotating fingering convection simulations in Sengupta and Garaud, 2018). As mentioned in Section 3.2, the initial conditions for each simulation have the fluid completely at rest, under a uniform magnetic field of unit strength, with small-amplitude, randomized perturbations in the \hat{T} and \hat{C} fields from which the instability can grow.

In the interest of probing the effect of magnetic fields on fingering convection specifically at low Prandtl number, as is relevant to astrophysical scenarios, all simulations have $\text{Pr} = 0.1$. This is not as low as the expected value of Pr in stellar or planetary interiors (where it can be several orders of magnitude smaller), but is numerically feasible and allows direct comparison to the existing body of low-Prandtl fingering convection simulations with no magnetic fields (Traxler et al., 2011; Brown et al., 2013; Sengupta and Garaud, 2018, etc.).

The density ratio in all simulations is $R_0 = 1.45$, and the compositional and magnetic diffusion parameters are fixed to $\tau = D_B = 0.1$. The base spectral resolution is 96 Fourier modes in

each direction, for a cubic domain with a side length of 100 in non-dimensional units (recall that the unit length in the chosen non-dimensionalization is d , given in Eq. 1.14). For simulations where the domain size is adjusted, the corresponding resolution is adjusted proportionally (i.e., doubling the vertical extent of the simulation domain also doubles the number of Fourier modes in the z -direction).

The H_B parameter, the coefficient of the Lorentz force term in the momentum equation, effectively controls the strength of the background magnetic field. The suite of simulations presented here tests a wide range of background field strengths, with $H_B \in \{0.01, 0.1, 1, 10, 100\}$. We test a background magnetic field oriented along both the vertical (z) direction, as well as along the horizontal (x) direction, and one case with an intermediate inclination. As we will see, the horizontal and vertical cases for the background field orientation both have significant effects on the nonlinear saturation and post-saturation behavior of the basic instability, but they yield distinctly different behaviors. We now focus on the qualitative results of the simulations, starting with the horizontal field cases, before developing a quantitative model for the behavior found in the vertical field cases.

4.1 Qualitative Results

4.1.1 Horizontal background fields

The simulations with horizontal background magnetic fields show rather surprising results. While the early growth of the instability matches the predictions from linear theory for all values of H_B (as described in Section 3.2), when $H_B \geq 0.1$, we find that after saturation, there is a significant departure from the behavior observed in the non-magnetic case. In Figure 4.1 we show the evolution over time of the kinetic and magnetic energies for a few of these simulations.

The $H_B = 0.01$ case is qualitatively indistinguishable from the non-magnetic case, showing the growth of the instability, its subsequent saturation, and the post-saturation, statistically stationary state characterized by homogeneous small-scale fingering convection. However, for $H_B \geq 0.1$, we find that although an initial saturation “peak” is reached in the kinetic energy, this local maximum

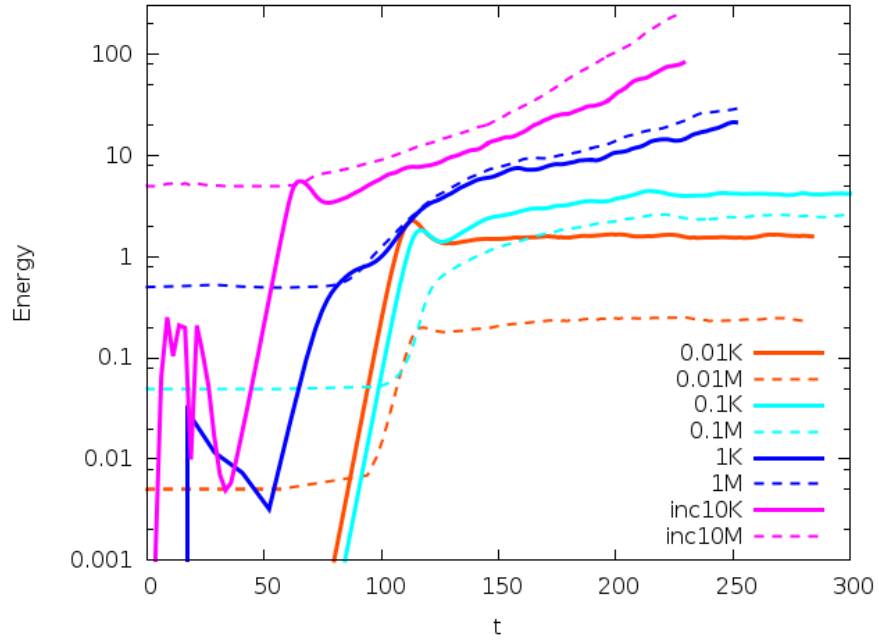


Figure 4.1: The evolution of the kinetic (solid lines, “K”) and magnetic (dashed lines, “M”) energies over time (in units of the thermal diffusion timescale) for horizontal magnetic field simulations with $H_B = 0.01$ (orange), $H_B = 0.1$ (cyan), and $H_B = 10$ (blue). Also plotted is a simulation with $H_B = 10$ and a field inclined 45° from the z -axis (purple, “inc”). The trajectory of the kinetic energy for the $H_B = 0.01$ case is qualitatively identical to that of the non-magnetic case.

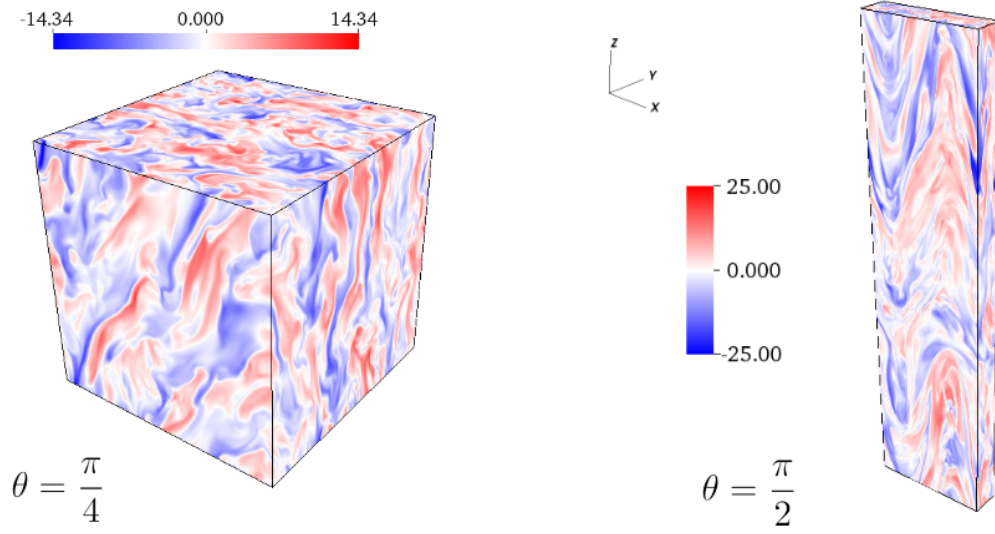


Figure 4.2: Sample visualizations of the vertical fluid velocity component for runs with $H_B = 10$. At left, we show a case with the background field inclined at an angle of $\theta = \pi/4$ from the z -axis, and at right we show a case with a fully-horizontal field (which required extending the vertical extent of the simulation domain considerably), long after the instability has surpassed the saturation “peak” of the initial instability.

is soon surpassed as both the kinetic and magnetic energies begin growing again. This subsequent growth eventually flattens out to reach a statistically stationary state, but one that has a significantly larger mean kinetic energy with respect to that of both the non-magnetic case as well as that of the initial saturation peak. By this stage, the vertical components of the fluid velocity and magnetic field dominate the contributions to the total kinetic and magnetic energy, respectively, despite the initial magnetic field having no vertical component.

The mechanism by which this process occurs is not immediately clear, but it may be the result of some sort of small-scale dynamo action. At the very least, these results indicate that horizontal magnetic fields can have a significant effect on magnetized fingering convection even at intermediate field strengths. Furthermore, this effect is able to significantly increase the amount of vertical fluid motion and turbulent transport of chemical species. This is contrary to the proposal of Charbonnel and Zahn (2007b) that significant horizontal magnetic field components might suppress mixing due to fingering convection in RGB stars.

Visualizations of cases with a background field inclined from the z -axis at $\theta = \pi/4$ and $\theta = \pi/2$ are shown in Figure 4.2. Qualitatively speaking, we see that for the inclined field case ($\theta = \pi/4$), the fingers respond to the direction of the magnetic field and form diagonal structures. This is consistent with the linear theory, and this snapshot was taken fairly early on in the simulation such that the linear regime was still prevalent. In the case of a fully-horizontal field, if we look at the structures that are formed long after the linear regime (i.e., long after the saturation “peak” of the initial instability is surpassed), we see the development of structures on domain-scale sizes.

There are a number of numerical difficulties associated with these simulations. Firstly, it seems that increasing the initial field strengths also increases the time it takes for the “dynamo” phase of the simulation to settle into a statistically stationary state, meaning that longer integration times are necessary. Second, it is necessary to ensure that the fingers do not become too vertically invariant as a result of self-interaction via the periodic boundary conditions (see the Appendix of Sengupta and Garaud, 2018), meaning taller and taller domains are required when large, coherent vertical structures develop (as was observed at late times in the $H_B = 1$ and $H_B = 10$ cases). Further progress in studying the effects of horizontal magnetic fields (and the late-time behavior) will have to heed these issues, but the results present an interesting new problem. We now focus on the case of a vertical background magnetic field, whose behavior is less complex than the horizontal case.

4.1.2 Vertical background fields

As detailed in Section 3.2, the early growth of the fingering instability in the DNSs with a vertical background field confirms the behavior predicted by the linear theory. The instability initially grows exponentially at a rate that is independent of H_B , and eventually settles into a statistically stationary, weakly-turbulent state of small-scale fingering convection. The principal effect of a vertical magnetic field is that as the strength of the background field increases via H_B , the fingers become more coherent and elongated along the vertical direction (see Figure 4.3). As a

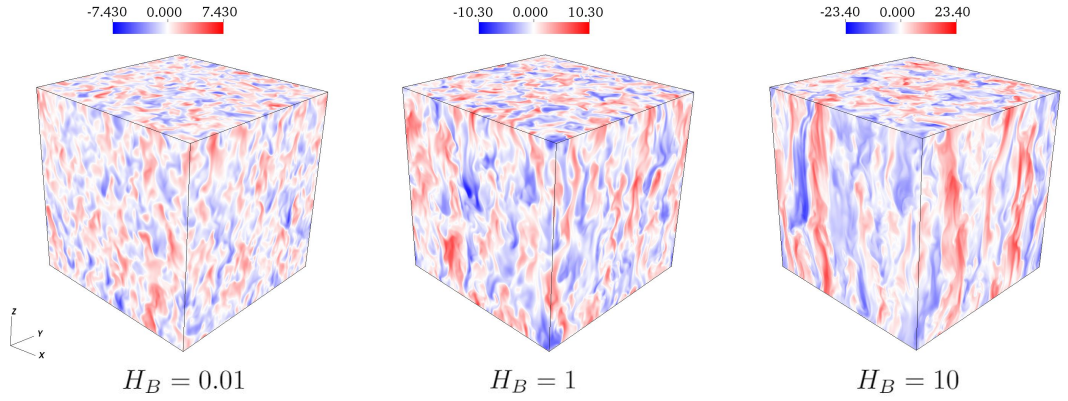


Figure 4.3: Visualizations of the vertical fluid velocity component during the post-saturation, statistically stationary state, for runs with a vertical background field and $H_B = 0.01$ (left), $H_B = 1$ (middle), and $H_B = 10$ (right). Increasing the strength of the magnetic field (via H_B) imparts greater vertical coherence to the fingering structures.

result, the temperature and compositional fluxes, as well as the r.m.s. vertical velocity, all increase significantly (see Figure 4.4).

Figure 4.3 shows visualizations of the vertical component of the fluid velocity once the fingering convection has reached a statistically steady state. The $H_B = 0.01$ case is indistinguishable from the non-magnetic case, with fingers that have a roughly unit aspect ratio. As H_B increases, we see an increasing anisotropy of the fingers, which become coherent over long vertical distances, as well as a marked increase in their vertical velocities. Furthermore, the onset of saturation seems to be more gradual for lower values of H_B , while the cases with large values of H_B have the fluid rapidly transition from laminar, vertical fingers into a saturated, turbulent state.

Qualitatively speaking, this can be explained by noting that increasing the field strength rigidifies the initial fingers vertically and delays saturation until a much higher r.m.s. vertical fluid velocity is reached. This increase in the vertical velocities within the fingers causes a substantial increase in the vertical turbulent compositional fluxes, as measured by the compositional Nusselt number Nu_C , defined by

$$\text{Nu}_C = 1 - \frac{R_0}{\tau} \langle \hat{u}_z \hat{C} \rangle = \frac{D_C}{\kappa_C}, \quad (4.1)$$

where $\langle \rangle$ denotes a volume average over the domain and D_C is the effective compositional diffusivity.

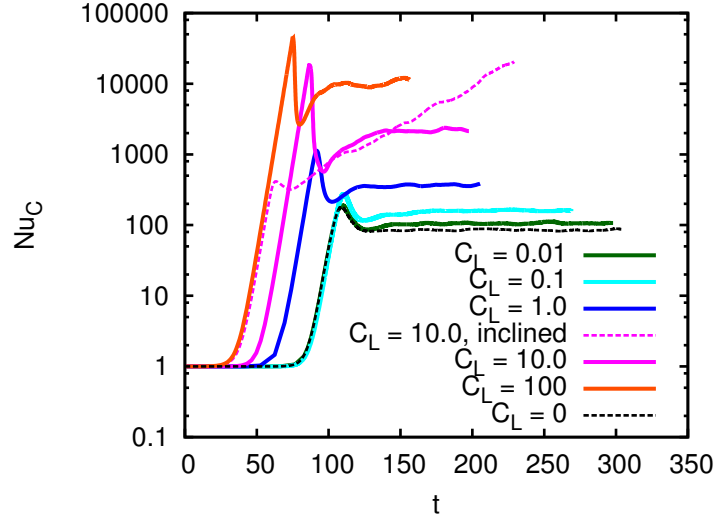


Figure 4.4: The compositional Nusselt number Nu_C (see Eq. (4.1)) as a function of time (in units of the thermal diffusion timescale) in simulations with a vertical field for various values of H_B . The dashed purple line shows the case with an inclined background field, and the black dashed-line shows a non-magnetic simulation ($H_B = 0$).

Figure 4.4 shows the evolution of Nu_C over time for each of the simulations. We see that stronger field strengths can significantly enhance the compositional transport by up to a few orders of magnitude compared with the non-magnetic case.

Also plotted in Fig. 4.4 is the evolution of Nu_C from the simulation with a background magnetic field inclined at 45° from the z -axis in the x - z plane, to offer a comparison between the vertical- and horizontal-field cases. As mentioned previously, the behavior for arbitrarily inclined background fields is more complex and will require further analysis, but preliminary results such as this confirm that the presence of a significant horizontal component in the background magnetic field can cause significant enhancements of compositional mixing.

4.2 Analytical model for the vertical field case

We now provide a simple quantitative model for the increase in thermocompositional fluxes caused by the presence of a vertical field. Previous work has shown that the mechanism responsible for saturation of ordinary fingering convection is the development of a shear instability between

adjacent up-flowing and down-flowing fingers (Radko and Smith, 2012; Brown et al., 2013), so an obvious explanation for our results is that the vertical magnetic field suppresses the shear instability. We now revisit the Brown et al. (2013) model, and include the effects of a vertical field.

In the hydrodynamic limit, Brown et al. (2013) assume that the fingers saturate when the growth rate $\hat{\sigma}$ of shear instabilities between up- and down-flowing fingers becomes commensurate with the growth rate $\hat{\lambda}_f$ of the fastest-growing modes of the basic fingering instability. That problem can be solved analytically using dimensional analysis, since the growth rate of the shearing instability must be $\hat{\sigma} \propto \hat{w}_f \hat{l}_f$ where \hat{w}_f is the velocity in the fingers, and \hat{l}_f is their horizontal wavenumber. Assuming that $\hat{\lambda}_f = C_B \hat{\sigma} = C_B \hat{w}_f \hat{l}_f$, where C_B is a universal constant, then provides an estimate for \hat{w}_f , namely $\hat{w}_f = \hat{\lambda}_f / C_B \hat{l}_f$. This was verified to hold by Sengupta and Garaud (2018), who found that $C_B \approx \frac{1}{2\pi}$.

To compute Nu_C , Brown et al. (2013) then assumed that

$$\langle \hat{u}_z \hat{C} \rangle \approx -K_B \frac{\hat{w}_f^2}{R_0(\hat{\lambda} + \tau \hat{l}_f^2)}, \quad (4.2)$$

where K_B is another constant and is of order unity. This then yields the formula

$$\text{Nu}_C = 1 + K_B \frac{\hat{w}_f^2}{\tau(\hat{\lambda} + \tau \hat{l}_f^2)} = 1 + \frac{K_B}{C_B^2} \frac{\hat{\lambda}_f^2}{\tau \hat{l}_f^2 (\hat{\lambda} + \tau \hat{l}_f^2)}, \quad (4.3)$$

which was fitted against data from numerical simulations to find that $\frac{K_B}{C_B^2} \approx 49$, which means $K_B \simeq 1.24$.

A vertical magnetic field, on the other hand, stabilizes the fingers against shear instabilities, so that larger velocities are required to trigger them. To see this, we studied formally the stability of a sinusoidal shear flow of the kind $\hat{w}_f \sin(\hat{l}_f x) \hat{e}_z$ (which mimics the flow within the finger elevator modes) in the presence of a constant vertical field of unit amplitude, by extending the Floquet analysis of Brown et al. (2013) (see their Appendix A). While the details of this calculation are presented in Appendix A of this thesis, the results are shown in Figure 4.5. We find that the growth rate of the shear instability $\hat{\sigma}$ now depends sensitively on the non-dimensional number

$$H_B^* = \frac{H_B}{\hat{w}_f^2}, \quad (4.4)$$

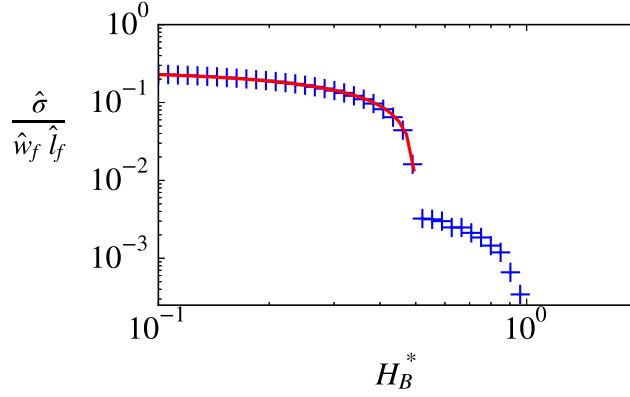


Figure 4.5: The non-dimensional growth rate of the shear instability $\hat{\sigma}$ as a function of H_B^* (blue crosses). The red line shows the fit given by Eq. (4.5).

which decreases as the velocity in the fingers increases.

There are two sets of modes unstable to shear – a slowly growing one, destabilized for $H_B^* < 1$, and a rapidly growing one, destabilized for $H_B^* < 0.5$. We fit the branch with larger growth rate as a function of H_B^* , getting

$$\frac{\hat{\sigma}}{\hat{w}_f \hat{l}_f} \simeq 0.42(0.5 - H_B^*)^{2/3}. \quad (4.5)$$

As in the Brown et al. (2013) model, we then assume that $\hat{\sigma}$ is of the order of the growth rate of the fingers $\hat{\lambda}_f$, according to

$$0.42\hat{w}_f\hat{l}_f(0.5 - H_B^*)^{2/3} = C_H\hat{\lambda}_f, \quad (4.6)$$

where C_H is a universal constant. By demanding that the $H_B^* = 0$ (hydrodynamic) limit reproduces the proportionality relation $C_B\hat{w}_f\hat{l}_f = \hat{\lambda}_f$, we determine that $C_H = (0.42)(0.5^{2/3})/C_B \approx 1.66$. Combining Eqs. (4.4) and (4.6), we can then express \hat{w}_f in terms of H_B , yielding a relation that is quartic in $\hat{w}_f^{1/2}$:

$$0.5\hat{w}_f^2 - H_B = \left(C_H \frac{\hat{\lambda}_f}{0.42\hat{l}_f}\right)^{3/2} \hat{w}_f^{1/2}. \quad (4.7)$$

We can immediately see two asymptotic regimes arising from this relation. The first is for very small H_B , where the velocity in the fingers simply approaches that of the Brown et al. (2013) hydrodynamic model. However, for very large H_B , the RHS term becomes negligible and the velocity

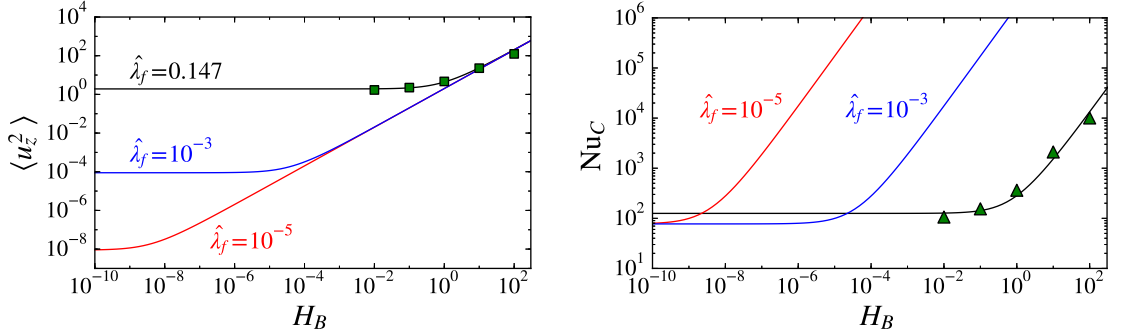


Figure 4.6: The volume-averaged squared vertical velocity $\langle u_z^2 \rangle$ (left, green squares) and compositional Nusselt number Nu_C (right, green triangles) as a function of H_B from the simulations. The different lines show the prediction from Eq. (4.7) for $\hat{\lambda}_f = 0.147$ (black), corresponding to the parameters in the simulations; $\hat{\lambda}_f = 10^{-3}$ (blue), representative of a white dwarf’s fingering convection environment; and $\hat{\lambda}_f = 10^{-5}$ (red), representative of an RGB star’s fingering convection environment.

in the fingers behaves roughly as $\hat{w}_f = \sqrt{2H_B}$. We call this the “magnetically-dominated” regime, which corresponds to equipartition between the kinetic energy of the fingers and the magnetic energy of the background field. Dimensionally, this implies that $\frac{1}{2}\rho_m w_f^2 = B_0^2/\mu_0$. We also see from Eq. (4.7) that the values of H_B where the transition between the two regimes occurs thus depends on the growth rate $\hat{\lambda}_f$ and horizontal wave number \hat{l}_f of the elevator modes, which are in turn dependent on the governing parameters (Pr , τ , R_0).

We can solve Eq. (4.7) numerically for \hat{w}_f as a function of H_B for various parameter values, the results of which are shown in Figure 4.6. With $\text{Pr} = \tau = D_B = 0.1$, and $R_0 = 1.45$, as in the numerical simulations, we have $\hat{\lambda}_f \approx 0.147$ and $\hat{l}_f \approx 0.666$, and find that the numerical results for $\langle \hat{u}_z^2 \rangle$ are well predicted by \hat{w}_f^2 computed from Eq. (4.7). We can see that the transition between the low- and high- H_B regimes for these parameter values occurs around $H_B = 1$.

However, in stellar interiors, the Prandtl number Pr (as well as τ) can be several orders of magnitude smaller than what we are able to simulate numerically, and in this $(\text{Pr}, \tau) \ll 1$ limit, we typically have (see Appendix B of Brown et al., 2013)

$$\hat{\lambda}_f \simeq \sqrt{\frac{\text{Pr} \tau (1/\tau - 1)}{R_0 - 1}} \simeq \sqrt{\frac{\text{Pr}}{R_0 - 1}} \ll 1, \quad (4.8)$$

which means the transition between low- and high- H_B regimes now occurs at a much smaller value of H_B . In Figure 4.6, we have also solved Eq. (4.7) for $\hat{\lambda}_f = 10^{-3}$ as well as $\hat{\lambda}_f = 10^{-5}$ (keeping $\hat{l}_f = 0.666$ fixed since \hat{l}_f remains $O(1)$ in the low-Pr limit), which are representative values of what we would expect in a WD or RGB star, respectively. These results show that the magnetically-dominated regime is $H_B \geq 10^{-4}$ for WD stars and $H_B \geq 10^{-8}$ for RGB stars. Thus, based on our estimates in Eqs. (1.25) and (1.26), it is reasonable to expect that fingering convection in such stars can be significantly affected by magnetic fields.

Using our model for \hat{w}_f^2 , we can finally compute the predicted turbulent compositional flux in magnetized fingering convection via

$$\text{Nu}_C = 1 + K_B \frac{\hat{w}_f^2}{\tau(\hat{\lambda} + \tau \hat{l}_f^2)}, \quad (4.9)$$

with the same value of K_B as in Brown et al. (2013). The results are summarized in the right panel of Figure 4.6, which shows Nu_C as a function of H_B , for the same three parameter regimes (numerical simulations, WD stars, and RGB stars).

We find that the value of Nu_C measured in the statistically stationary state in all of our simulations is well-predicted by our model. Crucially, we see that Nu_C scales like H_B in the magnetically-dominated regime, which can easily be understood since $\text{Nu}_C \propto \hat{w}_f^2 \propto H_B$ in that case. This means that Nu_C can increase by orders of magnitude depending on the background field strength. In fact, using Eqs. (4.8) and (4.3), together with the definitions of d and H_B , our model predicts that the turbulent compositional diffusivity due to magnetized fingering convection should be equal to

$$D_C \simeq 2K_B \frac{B_0^2}{\rho_m \mu_0} \sqrt{\frac{N_T^2 + N_\mu^2}{-N_T^2 N_\mu^2}}, \quad (4.10)$$

where $N_T^2 = \alpha g(dT_0/dz - dT_{\text{ad}}/dz)$ is the square of the temperature-based buoyancy frequency, $N_\mu^2 = -\beta g dC_0/dz$ is the square of the compositional buoyancy frequency (which is negative since the compositional field is destabilizing), and where we have assumed that $\hat{\lambda}_f \gg \tau \hat{l}_f$, which is typically the case for $R_0 \ll \text{Pr}^{-1/2}$. Equation (4.10) should hold as long as we remain in the magnetically-

dominated regime, which, as discussed earlier, corresponds to the limit $H_B \geq 10^{-4}$ in WDs, and $H_B \geq 10^{-8}$ in RGB stars.

Finally, note that the enhancement in the vertical finger velocity by magnetic fields can also affect heat transport, which is normally negligible in hydrodynamic fingering convection (Traxler et al., 2011). We predict using similar arguments that the equivalent Nusselt number for (potential) temperature should be

$$\text{Nu}_T = 1 + K_B \frac{\hat{w}_f^2}{\hat{\lambda} + \hat{l}_f^2}, \quad (4.11)$$

with a corresponding dimensional heat flux given by

$$F_T = -\rho_m c_p \kappa_T \frac{dT_0}{dz} + \rho_m c_p \kappa_T \left(\frac{dT_0}{dz} - \frac{dT_{\text{ad}}}{dz} \right) (1 - \text{Nu}_T). \quad (4.12)$$

With $\text{Nu}_T \gg 1$, we note the potential for transporting heat inward, as the right-hand term (which is usually small since Nu_T is ordinarily close to 1) can be made significantly negative.

5 Discussion

The linear theory, numerical simulations, and analytical model we have presented all provide significant, self-consistent evidence that magnetic fields undoubtedly affect the dynamics of astrophysical fingering convection. Perhaps the most important implication of these results is that significantly larger rates of compositional mixing can be attained, due to the ability of magnetic fields to enhance the r.m.s. vertical velocity after the fingers have saturated. This has obvious implications for the RGB stars abundance problem (Gratton et al., 2000) mentioned in Section 1.2.2. We can see from Figure 4.6 that even a moderate magnetic field of ~ 300 G (for which $H_B \sim 10^{-6}$) would increase the value of the turbulent mixing coefficient by two orders of magnitude compared with the non-magnetic case, which would then be sufficient to explain the observations (cf. Charbonnel and Zahn, 2007a). Such magnetic field strengths are not unreasonably large, and would indeed be likely in RGB stars. Although the analytical model behind this effect was limited to the case of a vertical field, we have also shown numerically that similar (or even larger) enhancements of the turbulent fluxes are likely if the field is inclined, so we expect our conclusions to be robust.

Another RGB mixing-related problem has the potential to be solved by these results. Some RGB stars with low metallicity and a surplus of carbon (so-called “carbon-enhanced metal-poor” stars) show peculiar abundances of Li and C which are only explained if the mixing coefficient associated with fingering convection decreases outward with increasing radius (Henkel et al., 2018). Since we have found the mixing coefficient D_C to depend on the magnetic field strength, which in turn most likely decreases with increasing radius within the star (e.g. if the field is of primordial

origin, or was created by a dynamo in a prior core-convective phase), we predict that D_C should decrease sharply with radius away from the hydrogen-burning shell. Thus, the magnetic field offers a natural explanation for the case of radially-dependent mixing as well. In general, it is clear that magnetic effects should not be neglected when considering fingering convection as a mechanism for various mixing processes in stellar evolution.

Our discovery of the intriguing behavior occurring when the magnetic field is sufficiently inclined presents a problem of both practical and theoretical importance. Developing an analytical model to explain the mechanism behind this behavior would likely complete our understanding of magnetic fingering convection in stellar environments, which could then lead to a conclusive resolution of the RGB “missing-mixing” problem. Also, it is possible that the addition of other relevant physical processes (e.g., rotation or shear) could lead to entirely different dynamics. Both the linear theory and the numerical tool developed in this work, **PADDIM**, can now serve as the foundation for which future projects may build upon.

Appendix A

Floquet theory for fingers in a vertical field

Here we will study the stability to shear of fingers in the presence of a vertical background magnetic field. We begin by setting up a two-dimensional sinusoidal shear flow in the x - z plane, a schematic of which is shown in Figure A.1, that mimics the flow within the fingers. We will take the unit velocity to be w_f , where w_f is the velocity of the fingers, and the unit length to be $1/l_f$, where l_f is the horizontal wave number of the fingers. Then, if we neglect buoyancy (thus neglecting evolution of the thermal and compositional fields) and diffusion (in both the velocity and magnetic

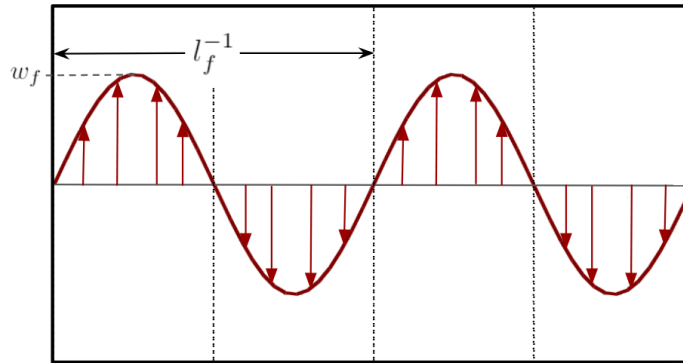


Figure A.1: Schematic of the two-dimensional sinusoidal shear flow considered in the Floquet analysis of magnetized shear between fingers.

fields), the non-dimensional governing equations are

$$\frac{D\mathbf{U}}{Dt} = -\nabla p + H_B^*(\nabla \times \mathbf{B}) \times \mathbf{B}, \quad (\text{A.1})$$

$$\frac{D\mathbf{B}}{Dt} = \nabla \times (\mathbf{U} \times \mathbf{B}), \quad (\text{A.2})$$

$$\nabla \cdot \mathbf{U} = 0, \quad (\text{A.3})$$

$$\nabla \cdot \mathbf{B} = 0, \quad (\text{A.4})$$

where D/Dt represents the Lagrangian (advective) derivative, \mathbf{U} is the fluid velocity, \mathbf{B} is the magnetic field, and p is the pressure. These equations yield the non-dimensional parameter

$$H_B^* = \frac{B_0^2}{\mu_0 \rho_m w_f^2}, \quad (\text{A.5})$$

where μ_0 is the magnetic permeability of vacuum, B_0 is the background field strength, and ρ_m is the density. We consider perturbations \mathbf{u} to the base sinusoidal flow such that

$$\mathbf{U} = \sin(x)\hat{\mathbf{e}}_z + \mathbf{u}, \quad (\text{A.6})$$

as well as perturbations \mathbf{b} to the background vertical magnetic field according to

$$\mathbf{B} = \hat{\mathbf{e}}_z + \mathbf{b}. \quad (\text{A.7})$$

Then, if we linearize the equations by dropping all terms which are nonlinear in the perturbations, we get

$$\frac{\partial \mathbf{u}}{\partial t} + \mathbf{u} \cdot \nabla (\sin(x)\hat{\mathbf{e}}_z) + (\sin(x)\hat{\mathbf{e}}_z) \cdot \nabla \mathbf{u} = -\nabla p + H_B^*(\nabla \times \mathbf{b}) \times \hat{\mathbf{e}}_z, \quad (\text{A.8})$$

$$\frac{\partial \mathbf{b}}{\partial t} = \nabla \times (\sin(x)\hat{\mathbf{e}}_z \times \mathbf{b}) + \nabla \times (\mathbf{u} \times \mathbf{B}_0), \quad (\text{A.9})$$

$$\nabla \cdot \mathbf{u} = 0, \quad (\text{A.10})$$

$$\nabla \cdot \mathbf{b} = 0, \quad (\text{A.11})$$

yielding the system

$$\partial_t u_x + \sin(x) \partial_z u_x = -\partial_x p + H_B^* (\partial_z b_x - \partial_x b_z), \quad (\text{A.12})$$

$$\partial_t u_z + \sin(x) \partial_z u_z + u_x \cos(x) = -\partial_z p, \quad (\text{A.13})$$

$$\partial_t b_x = -\partial_z (\sin(x) b_x) + \partial_z u_x, \quad (\text{A.14})$$

$$\partial_t b_z = \partial_x (\sin(x) b_x) - \partial_x u_x. \quad (\text{A.15})$$

The last two equations are redundant since $\nabla \cdot \mathbf{b} = \partial_x b_x + \partial_z b_z = 0$.

We now consider z -periodic perturbations of the form

$$\mathbf{u} = \hat{\mathbf{u}}(x) \exp(ikz + \sigma t), \quad \mathbf{b} = \hat{\mathbf{b}}(x) \exp(ikz + \sigma t), \quad p = \hat{p}(x) \exp(ikz + \sigma t), \quad (\text{A.16})$$

where σ is the growth rate and k is the vertical wave number of the perturbations. Substituting these into Eqs. (A.13) - (A.15) then transforms the z derivatives into $\partial_z \rightarrow ik$ and the temporal derivatives into $\partial_t \rightarrow \sigma$, yielding

$$\sigma \hat{u}_x + ik \sin(x) \hat{u}_x = -\partial_x \hat{p} + H_B^* (ik \hat{b}_x - \partial_x \hat{b}_z), \quad (\text{A.17})$$

$$\sigma \hat{u}_z + ik \sin(x) \hat{u}_z + \hat{u}_x \cos(x) = -ik \hat{p}, \quad (\text{A.18})$$

$$\sigma \hat{b}_x = -ik \sin(x) \hat{b}_x + ik \hat{u}_x. \quad (\text{A.19})$$

The divergence-free constraints on \mathbf{u} and \mathbf{b} become

$$\partial_x \hat{u}_x + ik \hat{u}_z = 0, \quad (\text{A.20})$$

$$\partial_x \hat{b}_x + ik \hat{b}_z = 0, \quad (\text{A.21})$$

which we can use to eliminate \hat{p} , \hat{u}_z , and \hat{b}_z . After some algebra, we arrive at the relations

$$\left(-\frac{i\sigma}{k} + \sin(x) \right) (\partial_x^2 \hat{u}_x - k^2 \hat{u}_x) + \hat{u}_x \sin(x) = H_B^* (\partial_x^2 \hat{b}_x - k^2 \hat{b}_x), \quad (\text{A.22})$$

$$\hat{u}_x = \left(-\frac{i\sigma}{k} + \sin(x) \right) \hat{b}_x \quad (\text{A.23})$$

Now we assume that \hat{u}_x and \hat{b}_x have the same periodicity as the base flow (i.e., with a fundamental horizontal wave number of one in this non-dimensionalization), so we expand \hat{u}_x and

\hat{b}_x in terms of a suitable basis, getting

$$\hat{u}_x = \sum_{n=-N}^N u_n e^{inx}, \quad \hat{b}_x = \sum_{n=-N}^N b_n e^{inx}. \quad (\text{A.24})$$

The sum over n should run from $-\infty$ to $+\infty$, but we have truncated it at $\pm N$ in anticipation of a numerical solution to the problem. Substituting these expansions into Eq. (A.23) yields

$$\sum_{n=-N}^N u_n e^{inx} = \left(-\frac{i\sigma}{k} + \frac{e^{ix} - e^{-ix}}{2i} \right) \sum_{n=-N}^N b_n e^{inx}, \quad (\text{A.25})$$

which we can project onto the m mode and get the relation

$$u_m = -\frac{i\sigma}{k} b_m + \frac{1}{2i} (b_{m-1} - b_{m+1}). \quad (\text{A.26})$$

Doing the same for Eq. (A.22), we get

$$\begin{aligned} \frac{i\sigma}{k} (m^2 + k^2) u_m - \frac{1}{2i} \left[((m-1)^2 + k^2) u_{m-1} - ((m+1)^2 + k^2) u_{m+1} \right] \\ + \frac{1}{2i} (u_{m-1} - u_{m+1}) = -H_B^* (m^2 + k^2) b_m. \end{aligned} \quad (\text{A.27})$$

We now eliminate the factors of i by employing the change of variables $v_m = iu_m$, and arrive at

$$kv_m - \frac{k}{2} (b_{m-1} - b_{m+1}) = \sigma b_m, \quad (\text{A.28})$$

$$-\frac{k}{2(m^2 + k^2)} \left[((m-1)^2 + k^2 - 1) v_{m-1} - ((m+1)^2 + k^2) v_{m+1} \right] - H_B^* b_m = \sigma v_m. \quad (\text{A.29})$$

Since we are looking for an expression for the growth rate σ of the shear instability, we do not need to find v_m or b_m explicitly. Rather, if we collect all $2N + 1$ modes of b_m and v_m into a vector $\mathbf{v} = (v_{-N}, \dots, v_N, b_{-N}, \dots, b_N)$, we can form an eigenvalue problem of the form

$$\mathbf{A}\mathbf{v} = \sigma\mathbf{v}, \quad (\text{A.30})$$

where \mathbf{A} is a matrix defined by the relations in Eqs. (A.28) - (A.29). For a given k , this eigenvalue problem can be solved numerically for σ , and because we are interested in the fastest-growing shear modes, we must maximize σ over k . Doing so for a range of H_B^* values then yields the results shown in Figure 4.5. Note that in this Appendix, we have defined σ in units of $w_f l_f$, so to match the non-dimensionalization of the main text (denoted by hatted quantities, resulting from the units in Eqs.

1.15 - 1.16), we multiply by $\hat{w}_f \hat{l}_f$. Thus, the non-dimensional growth rate of the shear modes here (σ) is related to the non-dimensional growth rate in the main non-dimensionalization ($\hat{\sigma}$) according to $\hat{\sigma} = \sigma \hat{w}_f \hat{l}_f$.

Bibliography

- P. G. Baines and A. E. Gill. On thermohaline convection with linear gradients. *Journal of Fluid Mechanics*, 37(2):289306, 1969.
- D. S. Balsara and J. Kim. A comparison between divergence-cleaning and staggered-mesh formulations for numerical magnetohydrodynamics. *The Astrophysical Journal*, 602(2):1079, 2004.
- J. U. Brackbill and D. C. Barnes. The effect of nonzero product of magnetic gradient and B on the numerical solution of the magnetohydrodynamic equations. *Journal of Computational Physics*, 35:426–430, May 1980.
- J. M. Brown, P. Garaud, and S. Stellmach. Chemical transport and spontaneous layer formation in fingering convection in astrophysics. *The Astrophysical Journal*, 768(1):34, 2013.
- C. Canuto, M. Hussaini, A. Quarteroni, and T. Zang. *Spectral Methods: Evolution to Complex Geometries and Applications to Fluid Dynamics*. Scientific Computation. Springer Berlin Heidelberg, 2007. ISBN 9783540307280.
- C. Charbonnel and J.-P. Zahn. Thermohaline mixing: a physical mechanism governing the photospheric composition of low-mass giants. *Astronomy & Astrophysics*, 467:L15–L18, May 2007a.
- C. Charbonnel and J.-P. Zahn. Inhibition of thermohaline mixing by a magnetic field in Ap star descendants: implications for the Galactic evolution of ${}^3\text{He}$. *Astronomy & Astrophysics*, 476:L29–L32, Dec. 2007b.

- M. Deal, S. Vauclair, and G. Vauclair. Thermohaline Instabilities Induced by Heavy Element Accretion onto White Dwarfs: Consequences on the Derived Accretion Rates. In *18th European White Dwarf Workshop.*, volume 469 of *Astronomical Society of the Pacific Conference Series*, page 435, Jan. 2013.
- P. A. Denissenkov. Numerical Simulations of Thermohaline Convection: Implications for Extra-mixing in Low-mass RGB Stars. *The Astrophysical Journal*, 723:563–579, Nov. 2010.
- P. A. Denissenkov, M. Pinsonneault, and K. B. MacGregor. Magneto-Thermohaline Mixing in Red Giants. *The Astrophysical Journal*, 696:1823–1833, May 2009.
- P. Garaud. What Happened to the Other Mohicans? The Case for a Primordial Origin to the Planet-Metallicity Connection. *The Astrophysical Journal Letters*, 728:L30, Feb. 2011.
- P. Garaud. Double-diffusive convection at low prandtl number. *Annual Review of Fluid Mechanics*, 50(1):275–298, 2018.
- P. Garaud, M. Medrano, J. M. Brown, C. Mankovich, and K. Moore. Excitation of gravity waves by fingering convection, and the formation of compositional staircases in stellar interiors. *The Astrophysical Journal*, 808(1):89, 2015.
- R. G. Gratton, C. Sneden, E. Carretta, and A. Bragaglia. Mixing along the red giant branch in metal-poor field stars. *Astronomy & Astrophysics*, 354:169–187, Feb. 2000.
- K. Henkel, A. I. Karakas, A. R. Casey, R. P. Church, and J. C. Lattanzio. Thermohaline Mixing in Extremely Metal-poor Stars. *The Astrophysical Journal Letters*, 863:L5, Aug. 2018.
- D. W. Hughes and N. O. Weiss. Double-diffusive convection with two stabilizing gradients: strange consequences of magnetic buoyancy. *Journal of Fluid Mechanics*, 301:383406, 1995.
- K. Julien, E. Knobloch, and M. Plumley. Impact of domain anisotropy on the inverse cascade in geostrophic turbulent convection. *Journal of Fluid Mechanics*, 837:R4, 2018.

- S. Kato. Overstable Convection in a Medium Stratified in Mean Molecular Weight. *Publications of the Astronomical Society of Japan*, 18:374, 1966.
- R. Kippenhahn, G. Ruschenplatt, and H.-C. Thomas. The time scale of thermohaline mixing in stars. *Astronomy & Astrophysics*, 91:175–180, Nov. 1980.
- G. M. Mirouh, P. Garaud, S. Stellmach, A. L. Traxler, and T. S. Wood. A New Model for Mixing by Double-diffusive Convection (Semi-convection). I. The Conditions for Layer Formation. *The Astrophysical Journal*, 750:61, May 2012.
- R. Moll and P. Garaud. The effect of rotation on oscillatory double-diffusive convection (semiconvection). *The Astrophysical Journal*, 834(1):44, 2017.
- S. A. Orszag and G. S. Patterson. Numerical simulation of three-dimensional homogeneous isotropic turbulence. *Phys. Rev. Lett.*, 28:76–79, Jan 1972.
- G. S. Patterson and S. A. Orszag. Spectral calculations of isotropic turbulence: Efficient removal of aliasing interactions. *The Physics of Fluids*, 14(11):2538–2541, 1971.
- R. Peyret. *Spectral Methods for Incompressible Viscous Flow*. Applied Mathematical Sciences. Springer New York, 2002. ISBN 9780387952215.
- T. Radko. A mechanism for layer formation in a double-diffusive fluid. *Journal of Fluid Mechanics*, 497:365–380, Dec. 2003.
- T. Radko. *Double-Diffusive Convection*. Cambridge University Press, 2013.
- T. Radko and D. P. Smith. Equilibrium transport in double-diffusive convection. *Journal of Fluid Mechanics*, 692:527, 2012.
- E. Rosenblum, P. Garaud, A. Traxler, and S. Stellmach. Turbulent Mixing and Layer Formation in Double-diffusive Convection: Three-dimensional Numerical Simulations and Theory. *The Astrophysical Journal*, 731:66, Apr. 2011.

- R. Schmitt, H. Perkins, J. Boyd, and M. Stalcup. C-salt: An investigation of the thermohaline staircase in the western tropical north atlantic. *Deep Sea Research Part A. Oceanographic Research Papers*, 34(10):1655 – 1665, 1987. ISSN 0198-0149.
- R. W. Schmitt, J. R. Ledwell, E. T. Montgomery, K. L. Polzin, and J. M. Toole. Enhanced diapycnal mixing by salt fingers in the thermocline of the tropical atlantic. *Science*, 308(5722):685–688, 2005.
- S. Sengupta and P. Garaud. The Effect of Rotation on Fingering Convection in Stellar Interiors. *The Astrophysical Journal*, 862:136, Aug. 2018.
- E. A. Spiegel. Semiconvection. *Comments on Astrophysics and Space Physics*, 1:57, Mar. 1969.
- E. A. Spiegel and G. Veronis. On the Boussinesq Approximation for a Compressible Fluid. *The Astrophysical Journal*, 131:442, Mar. 1960.
- R. J. Stancliffe, E. Glebbeek, R. G. Izzard, and O. R. Pols. Carbon-enhanced metal-poor stars and thermohaline mixing. *Astronomy & Astrophysics*, 464:L57–L60, Mar. 2007.
- S. Stellmach, A. Traxler, P. Garaud, N. Brummell, and T. Radko. Dynamics of fingering convection. part 2 the formation of thermohaline staircases. *Journal of Fluid Mechanics*, 677:554571, 2011.
- M. E. Stern. The salt-fountain and thermohaline convection. *Tellus*, 12(2):172–175, 1960.
- M. E. Stern. Collective instability of salt fingers. *Journal of Fluid Mechanics*, 35:209–218, 1969.
- M. E. Stern and J. S. Turner. Salt fingers and convecting layers. *Deep Sea Research and Oceanographic Abstracts*, 16(5):497 – 511, 1969. ISSN 0011-7471.
- H. Stommel, A. B. Arons, and D. Blanchard. An oceanographical curiosity: the perpetual salt fountain. *Deep Sea Research*, 3:152–153, Feb. 1956.
- R. Stothers and N. R. Simon. An Explanation for the Blue Sequence of Variable Stars. *The Astrophysical Journal*, 157:673, Aug. 1969.

- S. Théado and S. Vauclair. Metal-rich Accretion and Thermohaline Instabilities in Exoplanet-host Stars: Consequences on the Light Elements Abundances. *The Astrophysical Journal*, 744:123, Jan. 2012.
- S. Théado, S. Vauclair, G. Alecian, and F. LeBlanc. Influence of Thermohaline Convection on Diffusion-Induced Iron Accumulation in a Stars. *The Astrophysical Journal*, 704:1262–1273, Oct. 2009.
- M.-L. Timmermans, C. Garrett, and E. Carmack. The thermohaline structure and evolution of the deep waters in the Canada Basin, Arctic Ocean. *Deep Sea Research Part I: Oceanographic Research*, 50:1305–1321, Oct. 2003.
- A. Traxler, P. Garaud, and S. Stellmach. Numerically Determined Transport Laws for Fingering (“Thermohaline”) Convection in Astrophysics. *The Astrophysical Journal Letters*, 728:L29, Feb. 2011.
- J. Turner. The coupled turbulent transports of salt and and heat across a sharp density interface. *International Journal of Heat and Mass Transfer*, 8(5):759 – 767, 1965. ISSN 0017-9310.
- R. K. Ulrich. Thermohaline Convection in Stellar Interiors. *The Astrophysical Journal*, 172:165, Feb. 1972.
- S. Vauclair. Metallic Fingers and Metallicity Excess in Exoplanets’ Host Stars: The Accretion Hypothesis Revisited. *The Astrophysical Journal*, 605:874–879, Apr. 2004.
- F. C. Wachlin, S. Vauclair, and L. G. Althaus. Fingering convection in red giants revisited. *Astronomy & Astrophysics*, 570:A58, Oct. 2014.
- V. Zemsanova, P. Garaud, M. Deal, and S. Vauclair. Fingering Convection Induced by Atomic Diffusion in Stars: 3D Numerical Computations and Applications to Stellar Models. *The Astrophysical Journal*, 795:118, Nov. 2014.